



## RESEARCH ARTICLE

10.1002/2017JB014738

## Ambient Seismic Source Inversion in a Heterogeneous Earth: Theory and Application to the Earth's Hum

Laura Ermert<sup>1</sup> , Korbinian Sager<sup>1</sup>, Michael Afanasiev<sup>1</sup>, Christian Boehm<sup>1</sup>, and Andreas Fichtner<sup>1</sup><sup>1</sup>Institute of Geophysics, ETH Zurich, Zurich, Switzerland

## Key Points:

- We apply gradient-based ambient noise source inversion to long periodic "hum" cross correlations
- The inversion procedure fully accounts for heterogeneous Earth structure and finite-frequency sensitivity
- Hum sources appear persistent and narrowly localized at coasts or shelves and high bathymetry

## Supporting Information:

- Supporting Information S1

## Correspondence to:

L. Ermert,  
laura.ermert@erdw.ethz.ch

## Citation:

Ermert, L., Sager, K., Afanasiev, M., Boehm, C., & Fichtner, A. (2017). Ambient seismic source inversion in a heterogeneous Earth: Theory and application to the Earth's hum. *Journal of Geophysical Research: Solid Earth*, 122, 9184–9207. <https://doi.org/10.1002/2017JB014738>

Received 20 JUL 2017

Accepted 26 OCT 2017

Accepted article online 30 OCT 2017

Published online 27 NOV 2017

**Abstract** The sources of ambient seismic noise are extensively studied both to better understand their influence on ambient noise tomography and related techniques, and to infer constraints on their excitation mechanisms. Here we develop a gradient-based inversion method to infer the space-dependent and time-varying source power spectral density of the Earth's hum from cross correlations of continuous seismic data. The precomputation of wavefields using spectral elements allows us to account for both finite-frequency sensitivity and for three-dimensional Earth structure. Although similar methods have been proposed previously, they have not yet been applied to data to the best of our knowledge. We apply this method to image the seasonally varying sources of Earth's hum during North and South Hemisphere winter. The resulting models suggest that hum sources are localized, persistent features that occur at Pacific coasts or shelves and in the North Atlantic during North Hemisphere winter, as well as South Pacific coasts and several distinct locations in the Southern Ocean in South Hemisphere winter. The contribution of pelagic sources from the central North Pacific cannot be constrained. Besides improving the accuracy of noise source locations through the incorporation of finite-frequency effects and 3-D Earth structure, this method may be used in future cross-correlation waveform inversion studies to provide initial source models and source model updates.

**Plain Language Summary** The Earth's hum is a low-frequency, background seismic signal excited by the interplay of long periodic ocean waves with the Earth's solid crust. We present the first real-data application of a new localization technique for the sources of hum, which can be used for similar ambient sources in future studies. This technique can account for realistic wave propagation effects of seismic waves in the Earth. This is achieved by storing simulated responses of the Earth to impulsive sources, so-called Green's functions, in order to use them during localization. Our results confirm previous findings that the sources of the Earth's hum vary seasonally, occurring at Pacific coasts or shelves and in the North Atlantic during North Hemisphere winter, as well as South Pacific coasts and several distinct locations in the Southern Ocean in South Hemisphere winter. Our results also appear to indicate that hum sources are rather localized in space.

## 1. Introduction

We describe and apply a method to invert for the sources of ambient seismic noise. It has been developed with a twofold motivation: First, to serve as a preparatory step for cross-correlation waveform inversion as proposed by Tromp et al. (2010) and explored in synthetic studies by Hanasoge (2013a), Fichtner (2014), and Sager et al. (2017). Second, to provide improved constraints on the excitation of ambient seismic noise, while taking into account finite-frequency wave propagation through the laterally heterogeneous structure of the Earth. We introduce both motivations in the following. The method itself will be described in detail in section 2. It is based on forward modeling ambient noise cross correlations in a 3-D Earth and iteratively inverting them for the space-dependent power spectral density of the noise sources. Its application to the long-period background signal known as the Earth's hum will be covered in section 3. We close with a discussion of the results that both addresses their contribution to the current understanding of hum excitation and the further applicability of the method for ambient source inversion and ambient noise tomography.

## 1.1. Motivation I: Paving the Way for Ambient Noise Full-Waveform Inversion

The cross correlations of ambient seismic noise have become indispensable in seismic tomography (e.g., Chen et al., 2014; de Ridder et al., 2014; Fang et al., 2015; Green et al., 2017; Lin et al., 2008; Mordret et al., 2013;

©2017. The Authors.

This is an open access article under the terms of the Creative Commons Attribution-NonCommercial-NoDerivs License, which permits use and distribution in any medium, provided the original work is properly cited, the use is non-commercial and no modifications or adaptations are made.

Nakata et al., 2015; Nishida, Kawakatsu & Obara, 2008; Saygin & Kennett, 2012; Stehly et al., 2009; Yang et al., 2007; Zheng et al., 2011) and studies of attenuation and elastic (de) amplification (Bowden et al., 2015; Denolle et al., 2013; Harmon et al., 2010; Prieto et al., 2009). Current techniques are based on the assumption that cross correlations of the ambient seismic field converge to approximate interreceiver Green's functions (Boschi & Weemstra, 2015). For the equivalence of noise cross correlation and Green's function to hold, certain assumptions are required, namely equipartitioning of the noise wavefield (Gouédard et al., 2008; Sánchez-Sesma & Campillo, 2006; Weaver & Lobkis, 2004) or a favorable distribution of uncorrelated sources (Roux et al., 2005; Snieder, 2004; Wapenaar & Fokkema, 2006). Not least due to the complex dependence of the noise field on regional geographic and oceanographic conditions (e.g., Gualtieri et al., 2015; Sergeant et al., 2013; Stutzmann et al., 2012), these are not always fulfilled, which can lead to biases in both amplitude and traveltimes of the cross-correlation phases compared to interreceiver Green's functions and to the appearance of "spurious" arrivals (e.g., Froment et al., 2010; Halliday & Curtis, 2008; Tsai, 2009).

At the same time, earthquake tomography has attained new imaging capabilities through full-waveform inversion, which yields detailed images of Earth's interior structure on regional, continental, and global scale (e.g., Bozdağ et al., 2016; Chen et al., 2007; Fichtner et al., 2009; Simute et al., 2016; Tape et al., 2009, 2010). The ability to incorporate noise cross correlations into such models, as suggested by Afanasiev et al. (2016), could greatly benefit resolution in regions of low seismicity. However, since full-waveform inversion potentially translates waveform details into Earth structure, the heterogeneous distribution of noise sources must be taken into account to obtain correct sensitivity kernels and to avoid artifacts (e.g., Basini et al., 2013; Delaney et al., 2017; Fichtner, 2014; Hanasoge, 2013a; Sager et al., 2017).

Dropping the Green's function assumption and taking the full-waveform inversion approach to ambient noise tomography is expected to yield several benefits. It accounts for finite-frequency sensitivity, avoids bias due to heterogeneously distributed sources, and provides a way to quantify trade-offs (Sager et al., 2017). Furthermore, it enables us to consider spurious phases in the cross correlation arriving at high apparent velocity, as well as other waveform changes caused by persistent, localized sources (Brzak et al., 2009; Gaudot et al., 2016; Retailleau et al., 2017; Sadeghisorkhani et al., 2016; Tian & Ritzwoller, 2015). Finally, it permits the use of closely spaced station pairs (Lehuteur et al., 2017). Thus, it removes the requirement to select Green's function-like cross correlations and could greatly increase the amount of usable data (cf. data selection in Mordret et al., 2013; Pedersen et al., 2007; Stehly et al., 2009). In addition, the studies by Cupillard and Capdeville (2010) and Stehly and Boué (2017) suggest that it is crucial to account for ambient source distribution in order to evaluate cross-correlation amplitudes to derive anelastic attenuation.

Tromp et al. (2010), Hanasoge (2013a), Fichtner (2014), Ermert et al. (2016), and Sager et al. (2017) have discussed how to determine finite-frequency cross-correlation sensitivity kernels for noise sources. On this basis, we carry out the first inversion of observed ambient noise cross correlations for noise sources using a laterally varying Earth model, to pave the way for future applications of noise cross-correlation waveform tomography.

## 1.2. Motivation II: Finite-Frequency Noise Source Inversion With 3-D Structure

While the suggested method serves to prepare the ground for noise cross-correlation full-waveform inversion, it can be used in its own right to investigate ambient noise sources.

Besides their influence on ambient noise tomography, noise sources have been extensively studied with the aims of understanding their excitation mechanism (e.g., Haubrich & McCamy, 1969; Hillers et al., 2012; Juretzek & Hadziioannou, 2016; Landès et al., 2010; Stehly et al., 2006; Traer et al., 2012) and of using them as proxy for present and past ocean wave states or Antarctic sea ice cover (e.g., Aster et al., 2010; Ebeling & Stein, 2011; Donne et al., 2014; Stutzmann et al., 2009).

Previously developed localization methods for ambient sources include spectral analysis (e.g., Anthony et al., 2017; Bromirski, 2001; Bromirski & Duennebieber, 2002), polarization analysis (e.g., Chevrot et al., 2007; Schimmel et al., 2011; Schulte-Pelkum et al., 2004), cross correlation-based imaging (e.g., Ermert et al., 2016; Stehly et al., 2006; Tian & Ritzwoller, 2015; Yang & Ritzwoller, 2008), beamforming (e.g., Behr et al., 2010; Gal et al., 2015; Gerstoft & Tanimoto, 2007; Juretzek & Hadziioannou, 2016; Kurrle & Widmer-Schnidrig, 2006; Landès et al., 2010; Reading et al., 2014; Rhie & Romanowicz, 2004), migration of cross-correlation signals (Brzak et al., 2009; Dales et al., 2017; Retailleau et al., 2017), grid searches for fitting particular observables (Gaudot et al., 2016; Rhie & Romanowicz, 2006; Shapiro et al., 2006), and inversion based on simplified plane-wave models of noise

cross correlations (Harmon et al., 2010; Lehujeur et al., 2017; Sadeghisorkhani et al., 2016; Yao & van der Hilst, 2009). Nishida and Fukao (2007) inverted for the seasonal source of the Earth's hum using a model of cross correlations based on normal modes and a spherically symmetric Earth model.

Current challenges in locating ambient noise sources are (1) to incorporate finite-frequency sensitivity of noise cross correlations to spatially distributed sources, (2) to allow for close-by sources in the forward cross-correlation model by dropping the plane-wave assumption, and (3) to account for the three-dimensional, laterally heterogeneous structure of the Earth. While (1) and (2) have been addressed by the studies of Nishida and Fukao (2007), Brzak et al. (2009), and Stehly and Boué (2017), (3) is currently an outstanding problem. The inversion method proposed here addresses all three issues by using finite-frequency cross-correlation source sensitivity kernels in a three-dimensional Earth model. The computational cost of simulating the cross correlation is kept moderate through the use of a 3-D Green's function database. For our application case at long periods (see below), including 3-D elastic structure is not a primary concern. However, surface wave propagation effects currently pose important limitations to understanding aspects of the generation of microseisms (e.g., Juretzek & Hadziioannou, 2016). Thus, incorporating laterally varying Earth structure is intended as a methodological advance rather than a necessity for hum source inversion in particular.

### 1.3. Application to Earth's Hum

As case study, we apply the proposed inversion to the seasonal sources of the Earth's vertical-component hum. The Earth's seismic structure appears smooth to seismic waves at long periods of more than  $\approx 100$  s, and the seismic wavefield including surface waves is predicted rather well by 3-D tomographic models such as S40RTS (Ritsema et al., 2011) combined with crustal models that capture the ocean-continent distribution and major variations in crustal thickness. This allows us to invert for ambient sources of the hum without updating the structure of the Earth model. Moreover, Stehly et al. (2006) have shown that ambient noise can be observed coherently over very long distances, which makes noise source inversion an inherently global problem. With a global-scale application, we do not have to define an arbitrary limit to our model domain. Finally, the seasonally varying source distribution of the hum has been studied previously (Bromirski & Gerstoft, 2009; Nishida & Fukao, 2007; Rhie & Romanowicz, 2004), providing us with points of comparison to evaluate the proposed inversion procedure. There are furthermore several open questions regarding the excitation mechanism of the hum, which we will briefly review below. While in the present study our main focus is on the applicability of the inversion method to observed data, in section 5 we discuss the implications of our first results for hum sources.

We use the term "hum" here to refer to the low broad ridge of Peterson's New Low Noise Model extending from roughly 2 to 15 mHz (Peterson, 1993). The hum was first detected as continuously excited spheroidal normal modes at very quiet gravimeter and seismometer sites (Kobayashi & Nishida, 1998; Nawa et al., 1998; Suda et al., 1998; Tanimoto et al., 1998); subsequently, Kurrle and Widmer-Schmidrig (2008) succeeded in observing also continuously excited toroidal modes of similar amplitude as the spheroidal ones.

Early studies established that these signals could not be explained solely by the cumulative effect of small earthquakes (Suda et al., 1998). This was corroborated when seismic observations based on time series analysis (Ekström, 2001), beamforming (Rhie & Romanowicz, 2004), and linearized inversion of cross correlations (Nishida & Fukao, 2007) revealed seasonal modulation of the signal. Therefore, an atmospheric or oceanic source was suggested; Rhie & Romanowicz (2004, 2006) invoked coupling of ocean infragravity waves to the ocean floor as the most plausible mechanism. This view is now generally accepted, although questions remain about the contribution of atmospheric turbulences by resonant coupling (Nishida, 2014).

However, it is still debated by what precise physical mechanism infragravity waves couple to the seismic waves that propagate at far higher wave speeds than the ocean waves. Webb (2007, 2008) proposed to extend the double-frequency mechanism of Longuet-Higgins (1950) to longer periods. Fukao et al. (2010) emphasized the importance of shear sources, based on the findings of toroidal modes by Kurrle and Widmer-Schmidrig (2008), and proposed a mechanism of shear traction due to direct coupling of ocean waves and topographic irregularities of the same wavelength. Traer and Gerstoft (2014) suggested a mechanism similar to the one of Longuet-Higgins (1950), but in which the difference term of ocean wave frequencies, rather than their sum, determines the frequency of the seismic waves (see also Gerstoft & Bromirski, 2016). This would allow for hum excitation by oblique wave trains and would only occur in shallow water depths on the order of 100 m. Bromirski and Gerstoft (2009) and Traer et al. (2012) had previously reported that beam power time series

of the hum correlate with significant wave height time series in coastal, but not deep-water regions, indicating near-coastal areas as preferential hum source locations.

Unconvinced, Arduin et al. (2015) have recently demonstrated that observed hum power spectra can be quantitatively modeled by an excitation mechanism akin to that of the primary microseism (Hasselmann, 1963), with long-wavelength infragravity waves coupling to the seafloor due to bathymetric undulations or slopes. An important prediction of this is that shelf breaks and other locations of strong bathymetric gradient form narrow areas of preferential hum excitation.

Consequently, observational constraints are needed for the relative importance of coastal, shelf, and pelagic hum sources. While Bromirski and Gerstoft (2009) and Traer and Gerstoft (2014) emphasize the dominance of coastal source regions, Arduin et al. (2015) link hum excitation to shelf breaks, and Nishida and Fukao (2007), based on their inversion results, have argued that pelagic sources contribute as well.

In the present study our first goal is to further develop the ambient source inversion method and to apply it to observed data. Subsequently, we will discuss our findings and as well current possibilities and limitations of addressing the above questions with seismological observations.

## 2. Method

The proposed inversion method is based on the work of Tromp et al. (2010) and Fichtner (2014). Here we present a detailed derivation for the source inversion formulated in the time domain and with focus on the application to observed cross correlations. We will first introduce the forward model of ambient noise cross correlations, subsequently describe the optimization procedure, and finally discuss the computational approach that we developed and used for its application.

### 2.1. Forward Model

The forward model of cross correlations excited by noise sources goes back to the work of Woodard (1997) in helioseismology and was adapted to terrestrial seismology by various authors (e.g., Fichtner, 2014; Hanasoge, 2013b, 2013a; Tromp et al., 2010). The studies by Nishida, Kawakatsu, Fukao, et al., (2008) and Nishida (2014) are independent formulations of a similar approach and contain a range of representations for the cross correlation of ambient noise. Following this general idea, we regard the cross correlation itself as quantity which we can model, based on prior knowledge of the elastic medium and subsequently invert to improve upon the initial source distribution. This forward model requires no convergence of the cross correlation to an approximate interstation Green's function and is therefore also free of the assumptions required for Green's function retrieval.

The  $i$  component of ground velocity recorded at location  $\mathbf{x}$ ,  $v_i(\mathbf{x}, t)$ , can be expressed through a velocity Green's function  $G_{in}$  (e.g., Aki & Richards, 2002):

$$v_i(\mathbf{x}, t) = \int_{\oplus} [G_{in}(\mathbf{x}, \xi, t') * N_n(\xi, t')] (t) d\xi, \quad (1)$$

where we denote convolution by the asterisk and the  $n$ th component of the ambient seismic source field as a function of position  $\xi$  by  $N_n$ . The integration is over the volume of the Earth. Summation over repeated lowercase indices is implied. The continuous cross-correlation function of two noise recordings  $v_i(\mathbf{x}_1)$  and  $v_j(\mathbf{x}_2)$  with a duration of  $T$  is given by

$$\begin{aligned} C_{ij}(\mathbf{x}_1, \mathbf{x}_2, \tau) &= \frac{1}{T} \int_{-T/2}^{T/2} v_i(\mathbf{x}_1, t) \cdot v_j(\mathbf{x}_2, t + \tau) dt = [v_i(\mathbf{x}_1, -t) * v_j(\mathbf{x}_2, t)] (\tau) \\ &= \int_{\oplus} \int_{\oplus} [[G_{in}(\mathbf{x}_1, \xi_1) * N_n(\xi_1)] (-t) * [G_{jm}(\mathbf{x}_2, \xi_2) * N_m(\xi_2)] (t)] (\tau) d\xi_1 d\xi_2, \end{aligned} \quad (2)$$

where  $\tau$  is the cross-correlation time lag. We omit the normalization factor  $\frac{1}{T}$  from the convolutions denoted by asterisks for clearer notation. We assume that both the convolution in the representation theorem equation (1) and the convolution in equation (2) cover the finite time interval  $T$ . In the case of equation (1), this is analogous to assuming that a number of noise sources are active during  $T$  and then fall quiet. The use of the convolution theorem in equation (2) can be achieved by periodic continuation. Modeling  $C_{ij}$  as given by equation (2) with spatially varying source power is conceivable, but it is numerically very costly due to the necessity

of modeling long realizations for the noise fields from both sources  $N_n(\xi_1)$  and  $N_m(\xi_2)$ , (e.g., 20 days of numerically modeled noise in van Driel et al., 2015). Such models have only been computed for a small number of exemplary station pairs and/or in simplified wave propagation scenarios (Cupillard & Capdeville, 2010; Fichtner et al., 2017; van Driel et al., 2015). For the purpose of inverting a large number of observations in a realistic Earth model, however, we simplify the model by the following assumptions. First, we define ambient seismic sources as sources located at the Earth's surface, denoted by  $\partial\oplus$ . Thus, the volume integrals over  $\xi$  of equation (2) reduce to surface integrals. Second, one usually considers a stack of windowed correlations of continuous seismic data to reach better signal-to-noise ratios (Bensen et al., 2007; Seats et al., 2012). Therefore, we consider the long-term average of  $C_{ij}$  formed by stacking.

Contrary to the common practice of stacking noise cross correlations to retrieve an approximate Green's function, here we make no requirement of convergence and permit cross correlations to have an appearance that differs from interstation Green's functions. Therefore, the purpose of stacking here is to average out incoherent noise caused by coincidental correlation of instrumental and local (e.g., tilt) noise, so that we retrieve a signal from propagating seismic waves. If we assume that this incoherent noise is statistically uncorrelated, its expected contribution to the cross-correlation approaches zero for a large number of stacked windows.

Furthermore, we assume that constructive interference of signals from spatially separate sources tends to zero for a large number of stacked windows. This assumption can be summarized by writing an ensemble average  $\langle \cdot \rangle$  of the correlation of noise sources, which can be approximated by a time average:

$$\langle N_n(\xi_1, -t') * N_m(\xi_2, t') \rangle = S_{nm}(\xi_1, t) \cdot \delta(\xi_1 - \xi_2) \quad (3)$$

with the source autocorrelation  $S_{nm}(t)$ . This assumption is commonly applied (e.g., Hanasoge, 2013a; Snieder, 2004; Tromp et al., 2010; Wapenaar & Fokkema, 2006), both to keep the problem of noise cross correlations tractable and because one expects the correlation length of ocean-generated noise sources to be well below the seismic wavelength (Nishida & Fukao, 2007). We use it in the present study, but we will discuss in section 5 how the implementation that we propose below allows for an extension to sources with finite spatial correlation length.

To apply the argument of spatially uncorrelated sources by stacking, we consider the average and rearrange the convolutions

$$\begin{aligned} C_{ij}(\mathbf{x}_1, \mathbf{x}_2, \tau) &= \langle C_{ij}(\mathbf{x}_1, \mathbf{x}_2, \tau) \rangle \\ &= \left\langle \iint_{\partial\oplus} [G_{in}(\mathbf{x}_1, \xi_1, -t') * G_{jm}(\mathbf{x}_2, \xi_2, t')] \dots \right. \\ &\quad \left. \dots * [N_n(\xi_1, -t') * N_m(\xi_2, t')] (\tau) d\xi_1 d\xi_2 \right\rangle. \end{aligned} \quad (4)$$

Both Green's functions can be considered time invariant for the duration of the observation period, and consequently, the averaging is applied only to the multiple realizations of the noise sources  $N_n, N_m$ . With equation (3), equation (4) thus condenses to

$$C_{ij}(\mathbf{x}_1, \mathbf{x}_2, \tau) = \langle C_{ij}(\mathbf{x}_1, \mathbf{x}_2, \tau) \rangle = \int_{\partial\oplus} [G_{jm}(\mathbf{x}_2, \xi, t) * G_{in}(\mathbf{x}_1, \xi, -t) * S_{nm}(\xi, t)] (\tau) d\xi. \quad (5)$$

Using source-receiver reciprocity, we can rewrite the correlation wavefield as

$$C_{ij}(\mathbf{x}_1, \mathbf{x}_2, \tau) = \int_{\partial\oplus} [G_{mj}(\xi, \mathbf{x}_2, t) * G_{ni}(\xi, \mathbf{x}_1, -t) * S_{nm}(\xi, t)] (\tau) d\xi, \quad (6)$$

which is a useful representation for practical implementation. The cross correlation is now described by propagation of waves from sources at the seismic receiver locations  $\mathbf{x}_1$  and  $\mathbf{x}_2$ . Thus, the integral over  $\xi$  can be discretized and evaluated numerically if the Green's functions due to point sources injected at the receiver locations, and recorded at all source locations  $\xi$ , are provided.

The above model (equations (5) and (6)) does not account for commonly applied nonlinear preprocessing steps except those which recover the true signals of ground displacement  $v_i$ , for example, by diminishing meaningless noise such as recording glitches. Therefore, we apply minimal preprocessing in the application presented below.

## 2.2. Inversion

In equation (6),  $S_{nm}$  denotes the location-dependent source autocorrelation, and its frequency domain equivalent is the location-dependent source power spectral density (PSD). We will therefore refer to the model parameter as source PSD even though we may sometimes imply the time domain equivalent. We introduce the inversion procedure with a general misfit function and then extend it to the misfit function we use in the present work.

Inversion for  $S_{nm}$  will be performed by gradient-based iterative misfit minimization. The misfit function  $\chi$  quantifies the discrepancy between synthetic and observed cross correlations for one particular receiver pair  $r$ :

$$\chi = \chi \left( {}_r C_{ij}(S_{nm}), {}_r C_{ij}^o \right). \quad (7)$$

Given an observed noise cross-correlation function  ${}_r C_{ij}^o$ , the aim of the optimization problem is to find a space-dependent source PSD  $S_{nm}$  that minimizes the total misfit  $\mathcal{X}$  according to

$$S_{nm,\text{opt}}(\tau, \xi) = \underset{S_{nm}}{\operatorname{argmin}} [\mathcal{X}(S_{nm})] = \underset{S_{nm}}{\operatorname{argmin}} \left[ \sum_r \chi \left( {}_r C_{ij}(S_{nm}), {}_r C_{ij}^o \right) \right]. \quad (8)$$

The sum over  $r$  is over all station pairs of the data set. To perform the iterative inversion, we must first determine the (negative) gradient of the misfit function with respect to  $S_{nm}$ . In the following paragraphs, we drop the subscripts of  $S_{nm}$ , which refer to the components of the noise sources, as well as the subscripts of  $G_{mj}$ ,  $G_{ni}$ , in the interest of a more concise notation, but they are implied throughout. The misfit between the synthetic and observed cross correlations with respect to the source model  $S(\xi, \tau)$  may be influenced by source perturbations in the entire model domain and during the duration of the source autocorrelation. We therefore seek a way to express the misfit variation by two integrals, one over space  $\xi \in \partial\Theta \subset \mathbb{R}^2$  and the other either over frequency or equivalently over lag  $\tau \in [-\tau_{\max}, \tau_{\max}]$ . This expression serves to evaluate the sensitivity of the misfit variation to perturbations applied in any source location  $\xi$ , and at any lag  $\tau$ , by a source sensitivity kernel  $K$ :

$$\nabla_S \chi \delta S = \int_{\partial\Theta} \int_{-\tau_{\max}}^{\tau_{\max}} [K(\xi, t) * \delta S(\xi, t)](\tau) d\xi d\tau. \quad (9)$$

Here  $\nabla_S$  denotes the Fréchet derivative of the misfit functional with respect to  $S$ . Applying the chain rule, we obtain the directional derivative of  $\chi$  with respect to  $S$ :

$$\nabla_S \chi \delta S = \nabla_c \chi \delta_S C = \nabla_c \chi \nabla_S C \delta S. \quad (10)$$

In the above equation, both  $\nabla_c \chi$  and  $\nabla_S C$  are operators acting on the expressions to their right. The term  $\nabla_c \chi$  depends on the specific misfit used to compare the data and synthetics, and will be discussed below. The term  $\nabla_S C$  reflects the first-order change of the correlation function  $C$  with respect to  $S$  due to a small variation  $\delta S$ . To evaluate this first-order change, we make use of the linearity of the cross-correlation  $C(\tau)$  in the source term  $S$  (see equation (6) and write down its directional derivative directly, yielding

$$\nabla_S C(\tau) \delta S = \int_{\partial\Theta} (G(\xi, \mathbf{x}_2, t) * G(\xi, \mathbf{x}_1, -t) * \delta S(\xi, t))(\tau) d\xi. \quad (11)$$

Combining equations (11) and (10), we find that

$$\nabla_S \chi \delta S = \nabla_c \chi \int_{\partial\Theta} (G(\mathbf{x}_2, \xi, t) * G(\mathbf{x}_1, \xi, -t) * \delta S(\xi, t))(\tau) d\xi, \quad (12)$$

so that, by comparison with equation (9), we can anticipate that the derivative of the misfit function must contain the integral over lag:

$$\nabla_c \chi \cdot \circ = \int_{-\tau_{\max}}^{\tau_{\max}} f(\tau) \cdot \circ d\tau, \quad (13)$$

see equation A2 of Ermert et al. (2016) for the analogous argument in the frequency domain. The placeholder is used to denote the application of  $\nabla_c \chi$  to the following term. The sensitivity kernel for cross-correlation source inversion, for a lag-dependent misfit function  $\chi(\mathbf{x}_1, \mathbf{x}_2, \tau)$  can thus be expressed as

$$K(\xi, \tau) = f(\tau) \cdot (G(\mathbf{x}_2, \xi, t) * G(\mathbf{x}_1, \xi, -t))(\tau), \quad (14)$$

Equation (14) conveniently shows that the shape of the sensitivity kernel is determined by the cross correlation of the Green's functions between a source location and both receivers, regardless of the actual form of the misfit function  $\chi$ . In the Appendix A, we illustrate that in the special case of measuring the cross-correlation peak amplitude, the cross correlation of the Green's functions can be directly interpreted as sensitivity kernel, as suggested by Stehly and Boué (2017).

The kernel  $K$  shows the sensitivity of the total misfit to a unit change in source PSD depending on source location and correlation lag. The negative kernel thus provides a descent direction in which the model has to be updated in order to decrease and finally minimize the misfit function.

To minimize sensitivity to potentially undiscovered 3-D Earth structure, we use the logarithmic energy ratio  $A$  of the causal (positive lag) and acausal (negative lag) surface waves as basic measurement (Ermert et al., 2016). Denoting by  $w_+$  and  $w_-$  the symmetrically placed signal windows on the causal and acausal cross-correlation branches, respectively,  $A$  is defined as

$$A = \ln \left( \frac{\int [w_+(\tau)C(\tau)]^2 d\tau}{\int [w_-(\tau)C(\tau)]^2 d\tau} \right). \quad (15)$$

In the logarithmic energy ratio, interstation structural effects largely cancel due to source-receiver reciprocity, so that minimal trade-offs with elastic focusing and attenuation are expected. The synthetic misfit study by Sager et al. (2017) corroborates this intuition numerically in a 2-D setting.

While the misfit function  $\chi$  in its most general form depends on both source location and frequency, the measurement  $A$  has no explicit frequency dependence. We therefore modify it here to include spectral information by equipping it with a prefilter  $H(\tau)$ .

$$A_l = \ln \left( \frac{\int [w_+(\tau) \cdot H_l(\tau) * C(\tau)]^2 d\tau}{\int [w_-(\tau) \cdot H_l(\tau) * C(\tau)]^2 d\tau} \right) = \ln \left( \frac{E_{l,+}}{E_{l,-}} \right) \quad (16)$$

Subsequently, we may combine prefilters  $H_l(\tau)$ , covering a specific frequency band, by summation and evaluate the misfit between the measurement on the synthetic correlations,  $A_l$ , and that on the observed ones,  $A_l^o$ , using an  $L_2$  norm:

$$\chi = \frac{1}{2} \sum_l [A_l - A_l^o]^2. \quad (17)$$

For practical purposes, the filters  $H_l(\tau)$  should be zero phase to avoid a separate treatment of the causal and acausal branches. Writing the filtered windowed cross-correlation trace as

$$C_{l,+} = [w_+(\tau) \cdot H_l(\tau) * C(\tau)] \quad (18)$$

and  $C_{l,-}$  analogously, the misfit derivative with respect to the cross correlation for one particular frequency band is

$$\nabla_c \chi_l \cdot \circ = \int_{\tau_{\max}}^{\tau_{\max}} [A_l - A_l^o] \cdot \left[ \frac{w_+(\tau) \cdot H_l(\tau) * C_{l,+}}{E_{l,+}} - \frac{w_-(\tau) \cdot H_l(\tau) * C_{l,-}}{E_{l,-}} \right] \cdot \circ d\tau \quad (19)$$

which has the anticipated form of equation (13). The space-dependent sensitivity kernel for one particular frequency band is therefore

$$K_l(\xi, \tau) = 2 \cdot [A_l - A_l^o] \cdot \left[ \frac{w_+(\tau) \cdot H_l(\tau) * C_{l,+}}{E_{l,+}} - \frac{w_-(\tau) \cdot H_l(\tau) * C_{l,-}}{E_{l,-}} \right] \cdots \quad (20)$$

$$\cdots \cdot [G(\mathbf{x}_2, \xi, t) * G(\mathbf{x}_1, \xi, -t)](\tau).$$

This kernel depends on space and cross-correlation lag and, after discretization, has dimensions of the number of source locations by the number of cross-correlation samples. Since we do not expect to resolve each frequency of the source PSD, it is convenient to parameterize the source PSD by a number of spectral basis functions  $s_k$ . We express this parameterization in the frequency domain for better readability (taking up subscript indices  $nm, ij$  again):

$$\tilde{S}_{nm}(\omega, \xi) = \int S_{nm}(\tau, \xi) \cdot \exp(-i\omega\tau) d\tau = \sum_k s_k(\omega) \cdot S_{k, nm}(\xi) \quad (21)$$

where  $\omega$  is angular frequency. To illustrate this in a straightforward manner, we choose nonoverlapping basis functions  $s_k(\omega) = \tilde{H}_k(\omega)$  that match the filters  $H_l(\tau)$  which are applied to the cross-correlation data. In this parameterization, the forward model becomes

$$C_{ij}(\mathbf{x}_1, \mathbf{x}, \tau) = \frac{1}{2\pi} \sum_k \iint_{\partial\Theta} \tilde{H}_k(\omega) \cdot \tilde{G}_{mj}(\xi, \mathbf{x}_2, \omega) \cdot \tilde{G}_{ni}^*(\xi, \mathbf{x}_1, \omega) \exp(i\omega\tau) d\omega \cdot S_{k, nm}(\xi) d\xi \quad (22)$$

where  $\tilde{G}$  denotes the frequency domain equivalent of  $G$ . The space-dependent source sensitivity kernel for one particular spectral basis and the corresponding frequency band is then

$$K_{k, l, nm}(\xi) = \nabla_c \chi_l \frac{1}{2\pi} \int \tilde{H}_k(\omega) \cdot \tilde{G}_{mj}(\xi, \mathbf{x}_2, \omega) \cdot \tilde{G}_{ni}^*(\xi, \mathbf{x}_1, \omega) \exp(i\omega\tau) d\omega, \quad (23)$$

where the term  $\nabla_c \chi_l$  includes the integral over  $\tau$  from equation (13). The variation of misfit for one station pair is found by a double sum over all filters and basis functions, in analogy to equation (9).

$$\nabla_s \chi \delta S_{nm} = \sum_k \sum_l \int_{\partial\Theta} K_{k, l, nm}(\xi) \cdot \delta S_{k, nm} d\xi, \quad (24)$$

where instead of the full spectrum we now update a small number of scalar weights  $S_{k, nm}$  pertaining to the spectral basis functions. The double sum over  $k, l$  indicates that each filtered measurement  $A_l$  may update the weights for each basis function. However, since we have assumed that the basis functions are well separated and match the filters  $H_l(\tau)$ , we may assume that each filtered measurement contributes predominantly to the update of the spectral weight  $S_{k, nm}(\xi)$  of the corresponding basis function  $H_k(\omega)$ . One can then simplify equation (24) as

$$\nabla_s \chi \delta S_{nm} \approx \sum_l \int_{\partial\Theta} K_{l, nm}(\xi, \tau) \cdot \delta S_{l, nm} d\xi. \quad (25)$$

Based on the sensitivity kernel  $K_l$ , we can now run iterative inversions for  $S_{nm}$ .

The misfit variation  $\nabla_s \chi$  may require updates that result in negative source PSD. Since the PSD is nonnegative by definition, we introduce a nonnegativity constraint. Evaluating the projected descent direction yields the update for step  $s + 1$ :

$$S_{s+1}(\xi) = \max(S_s(\xi), 0), \quad (26)$$

(Hinze et al., 2008), where  $l_s$  is optimal step length and  $h_s$  is the update for step  $s$ .

### 2.3. Using Precomputed Wavefields

The evaluation of both the forward model (equation (6)) and the sensitivity kernels (equation (20)) requires the modeling of Green's functions between the seismic receivers and all possible source locations for realistically heterogeneous Earth models. However, computing synthetic seismograms numerically using 3-D solvers of viscoelastic wave propagation (e.g., Gokhberg & Fichtner, 2016; Komatitsch & Tromp, 2002a) is a computationally intensive task, which would additionally have to be repeated in each iteration.

To reduce the computational requirements, we devised a noise source inversion procedure based on a database of precomputed wavefields. The idea to considerably reduce computational cost by using a wavefield database has previously been applied to different problems in seismology, such as adjoint tomography (e.g., Nissen-Meyer et al., 2007; van Driel et al., 2015) and earthquake source inversion (e.g., Hejrani et al., 2017; Lee et al., 2011). Equation (6), which is related by source-receiver reciprocity to the correlation forward model equation (5), allows us to calculate the required Green's functions efficiently by placing sources at the locations of receivers and recording the resulting wavefield at a dense grid of possible source locations. Figure 1 shows a schematic illustration. Such a precomputed wavefield can be obtained from any wave propagation solver. The specifics of the wavefield used in this study are detailed in section 3.3. Once the wavefield has been computed and stored for all source locations, it can be used to construct both the forward model (equation (6)) and the source sensitivity kernels (equation (20)) by approximating the spatial integral with a sum over the integrand for discrete source locations. For instance, given a precomputed database, the cross correlation for one station pair in the global inversion presented below (section 3) can be forward modeled within minutes on a single CPU. Due to the restriction of ambient seismic sources to the Earth's surface, storage sizes of the Green's function database are manageable; on the order of 10 GB per receiver in our specific application.

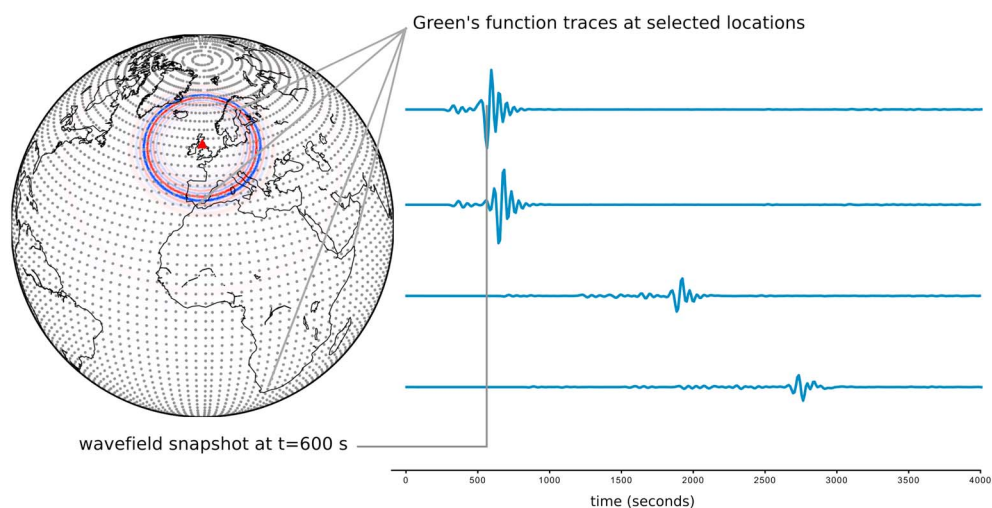


**Figure 1.** An illustration of the precomputed wavefield approach. The map on the left shows a time snapshot of the wavefield emanating from a point source at Eskaldemuir, Scotland (indicated by the red triangle). The gray dots show an illustrative  $5^\circ \times 5^\circ$  grid of source locations. A grid with finer resolution of 30 km is used for the actual inversion but cannot be represented visually. The seismograms on the right are individual Green's functions at the indicated locations. The vertical dashed line indicates the timing of the snapshot.

Using this approach, the computational cost of evaluating the forward model, although low, scales with the number of receiver pairs. In contrast, the cost of the approach described by Fichtner (2014), Sager et al. (2017), and Tromp et al. (2010), which recalculates Green's functions at each iteration for both the forward field and kernels, scales with the number of reference stations. Thus, for very large data sets (in the current example, on the order of 1 million cross correlations), the latter approach becomes more efficient again.

### 3. Case Study: Global Sources of the Earth's Hum

As a first feasibility study for our 3-D ambient source inversion method, we chose the vertical-component sources of the long-period background signal known as the Earth's hum (Kurrle & Widmer-Schmidrig, 2006; Nawa et al., 1998; Nishida et al., 2000; Suda et al., 1998; Tanimoto et al., 1998, and others). In the following, we will describe the data set, the inversion setup, and the resulting hum source models.

#### 3.1. Data Set

The Earth's hum is a low-amplitude, long-period signal with typical ground displacements not exceeding a few micrometers. Here we focus on periods between 120 and 330 s, where sensor characteristics make observation rather susceptible to instrumental noise. Furthermore, they are particularly affected by barometric variations and tilt. Therefore, Kurrle and Widmer-Schmidrig (2006) argued that propagating hum could only be observed at the quietest stations. Indeed, Nishida and Fukao (2007) used only the 54 quietest very high gain broadband stations of the GSN network.

To retrieve a meaningful cross-correlation signal despite these limitations, we compiled a global data set from all permanent stations that operate STS-1 broadband seismometers with a flat frequency response up to 360 s (Wielandt & Streckeisen, 1982), summarized under network code `_STS-1` in the IRIS data management center ([ds.iris.edu/mda/\\_STS-1](https://ds.iris.edu/mda/_STS-1)). We retrieved data for 146 stations during the years 2004–2013. Station locations are shown on the map in Figure 2.

A detailed description of the data compilation and processing is provided in Ermert et al. (2016) where we used the data for a ray-based map of global hum sources. Data processing was performed with a cross-correlation tool based on Obspy (Beyreuther et al., 2010). Instead of explicitly excluding earthquake signals, we normalized each cross-correlation window by the energy of both traces, downweighting the contribution of any large-amplitude signals. This processing diverges from our forward model due to the addition of the normalization term. We will return to this aspect in section 5. The maximum correlation lag was set to 3 h and 20 min, to capture both minor- and major-arc Rayleigh waves, although in the present application, we limit the inversion to minor-arc observations. Rather than forming stacks by month (e.g., stacking each December through years 2004 to 2013) as in Ermert et al. (2016), here we compiled two seasonal cross-correlation stacks

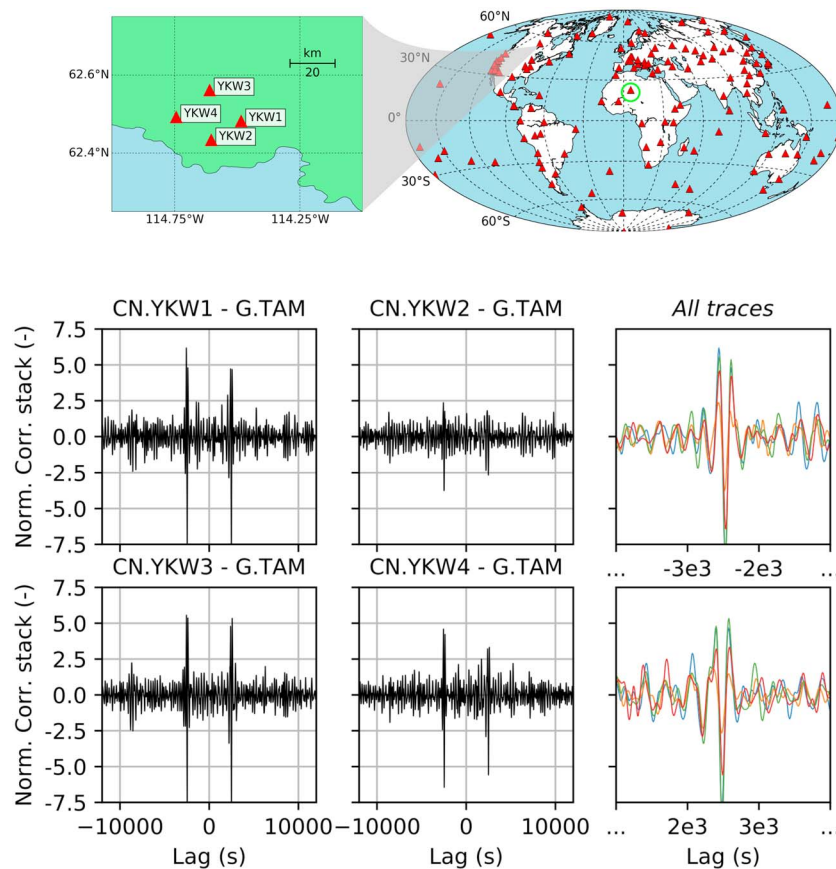


**Figure 2.** Observational uncertainty was assessed by comparing correlations from the (top left) four broadband stations of the Yellowknife seismic array with reference stations worldwide. (top right) This example shows correlations with respect to G.TAM in Algeria, at a distance of  $\sim 9,000$  km (marked by green circle on the map of global station distribution of the data set). (left and middle columns) The correlation traces for each of the four Yellowknife stations. (right column) An overlay of the four traces, centered on the causal and acausal R1 wave group. While phases are rather consistent, amplitudes and relative amplitudes vary more. However, the acausal correlation branch shows consistently higher amplitudes.

for improved signal-to-noise ratio (SNR), one for North Hemisphere (NH) winter and one for South Hemisphere (SH) winter. Each of them spans 3 months out of the 10 years (i.e., December, January, February 2004–2013 for NH winter and June, July, August 2004–2013 for SH winter). For the SH winter inversion, we excluded nine stations from the cluster of STS-1 stations in California to avoid overemphasis of the southward facing sensitivity of this cluster (see section 5 and Figure S5 in the supporting information).

### 3.2. Data Quality Assessment

To avoid overfitting, we performed a careful assessment of the data quality before the iterative inversion. Since we do not require convergence to an approximate Green's function, selection criteria commonly employed for ambient noise tomography, such as symmetry of the cross-correlation function (Stehly et al., 2009), are not meaningful for our assessment. Instead, we invoke a consistency criterion, namely the comparison of cross correlations at neighboring stations with respect to a distant reference station. We utilized the broadband receivers of the Canadian Yellowknife array to investigate the reliability of the measurement  $A_i$  (equation (16)). These receivers are nearly colocated with a maximum distance of less than 10 km, much less than the investigated seismic wavelengths that are on the order of several hundreds of kilometers. Therefore, approximately synchronous cross correlations of data from the sensors with respect to a distant reference station should produce equal values of  $A_i$ , except for effects caused by (1) instrumental noise and (2) highly site-specific effects, for example, tilt induced by barometric pressure changes at a distance of few kilometers around the station. Figure 2 illustrates the quality assessment. It shows the correlations of the four Yellowknife broadband stations

with respect to reference station G.TAM in Algeria, for illustrative purposes stacked over the years 2006–2008, and band-pass filtered between 100 and 330 s. Figures 2 (left column) and 2 (middle column) show the four correlation traces. The top and bottom plots of Figure 2 (right column) are zoomed onto their acausal and causal R1 arrival, respectively. The phases of the four traces match well, while their absolute amplitudes differ.  $A_i$  ranges between  $-0.15$  and  $-0.34$ , with relative amplitudes showing a consistently higher excitation of the acausal Rayleigh wave, but at varying levels of asymmetry. In addition, the correlations show varying SNRs.

To assess these differences more quantitatively, we measured  $A_i$  for the Yellowknife stations YKW1 and YKW3 with respect to all available reference stations in the data set, this time on the seasonal stacks used for the inversion. (YKW2 and YKW4 were not used, because they were discontinued in 2009, hence contributing less to the seasonal stacks.) The average variance between the two measurements is the best estimate we can obtain for the uncertainty of our measurement due to data gaps, tilt noise, and other unknown factors. The mean of (two-station) variances is 0.3 for the NH winter and 0.2 for the SH winter. The quality of these correlation traces is good as evidenced by their consistent phases. Therefore, amplitude deviations such as these are to be expected as observational error. Our estimate of the measurement uncertainty is, however, limited by the fact that we can only obtain it from this particular location.

For the limited comparisons available, we found hardly any correlation between high SNR and high consistency between the measurements. Therefore, we did not use an SNR criterion for data selection. Data gaps are a common problem with the 10 year, continuous global data set. Therefore, we applied a selection criterion of a minimum number of 320 stacked windows. In addition, we discarded all data where the causal and acausal observation windows, defined as 1,200 s Hann windows centered on the arrival of a Rayleigh wave with a group velocity of 3,700 km/s, overlapped due to a short interstation distance. This effectively resulted in removing most station paths within California from the data set.

### 3.3. Inversion Setup

Based on the developments in section 2 and the observed cross-correlation data set, we invert for the optimal source distribution  $S_{i,zz}(\xi)$  both during NH and SH winter using the filtered logarithmic amplitude measurement  $A_i$  (equation (16)). We use one single broad period range from  $\approx 130$  to 330 s, and parameterize the spectrum of  $S_{nm}(\xi, \tau)$  by a Gaussian spectrum approximately matching the filter  $H(\tau)$  that selects this period band, obtaining the optimal space-dependent hum source PSD  $S_{k,nm}(\xi)$  without varying the shape of the spectrum.

We assume that the influence of horizontally acting noise sources on the vertical-vertical cross correlation is negligible. Hence, we invert for  $S_{k,zz}(\xi)$  using the  $C_{zz}$ -component. This choice is not least dictated by the data themselves, as we did not retrieve clear signals on the horizontal-component correlations. We specifically target minor-arc Rayleigh surface waves ( $R_1$ ). Considering major-arc Rayleigh waves, body waves, or waves arriving at spurious lag times is beyond the scope of this study. In accord with equation (6), we only permit sources to act at the Earth's surface.

For recomputing the Green's functions, we use spectral-element solver SPECFEM3D\_GLOBE (Komatitsch & Tromp, 2002a; 2002b). We choose S40RTS (Ritsema et al., 2011) as mantle model, complemented by the attenuation model of PREM (Dziewoński & Anderson, 1981) and a smoothed version of the crustal model CRUST2.0 (Bassin et al., 2000). The simulations include gravity, rotation, ellipticity, ocean load, and topography. For simplicity, receivers are located at sea level. Simulations are accurate to  $\approx 20$  s period (Specfem developers, 2015), which will permit later reuse of the Green's function database for higher-frequency studies. For the numerical simulations, we successively place a point source at the location of each of the 146 STS-1 receivers in our data set (see Figure 2) and compute 8 h long seismograms that are recorded at all noise source locations. The long simulation duration of 8 h was chosen to obtain cross correlations with sufficient overlap of the Green's functions and because multiple-orbit surface waves all contribute to the cross correlation and the source sensitivity kernel. An example illustrating the effect of simulation duration is shown in Figure S1 of the supporting information. The total computation time of all 146 point source simulations was approximately 3,000 node hours on the *Piz Daint* cluster of the Swiss National Supercomputing Centre.

For the Green's function database, we resample the simulated wavefields spatially on an equal-distance grid with 30 km spacing at Earth's surface and temporally at an interval of 10 s. Using the Green's function database,

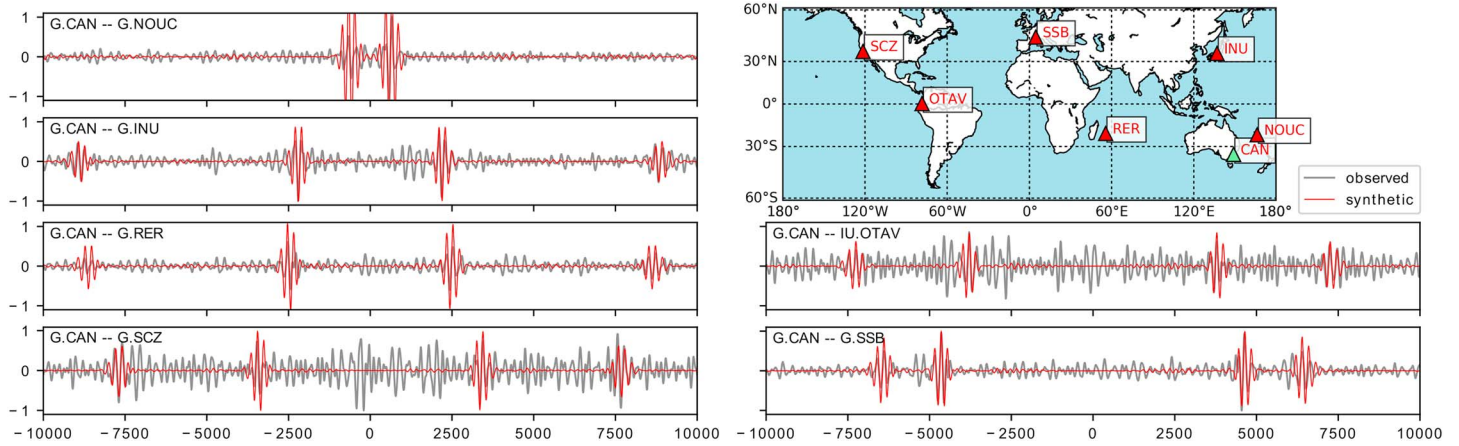


**Figure 3.** Comparison between normalized synthetic and observed cross correlations at receiver pairs with respect to reference station G.CAN. Station locations are shown on the map. The synthetics are computed with a homogeneous starting model for the ambient source.

we model all observed cross correlations according to equation (6). As starting model for the source PSD, we choose a spatially homogeneous distribution with a Gaussian spectrum:

$$S_{l,zz}(\xi) = \text{const}, \quad s_l(f) = e^{-(f-f_c)^2/(2\sigma_f)^2} \cdot \frac{1}{s}, \quad f = \frac{\omega}{2\pi}. \quad (27)$$

The spectrum is centered at  $f_c = 5$  mHz and has a standard deviation of  $\sigma_f = 1$  mHz. An exemplary collection of observed and initial synthetic correlations is shown in Figure 3. In each iteration, we evaluate the misfit of the logarithmic signal energy ratio  $A_l$  between synthetic and observed cross correlation. Following the computation of sensitivity kernels, the weights  $S_{k,zz}$  are then updated relative to a constant reference level during the inversion, because the measurement used is insensitive to absolute amplitude.

A representative example of a sensitivity kernel is shown in Figure 4. All source kernels share some important characteristics that are in contrast to sensitivity kernels for Earth structure:

1. The largest sensitivity is located in two Fresnel zone-like patterns behind and not in between the station pairs.
2. Sensitivity is antisymmetric, that is, positive behind one and negative behind the other station, as a result of the logarithmic ratio measurement.

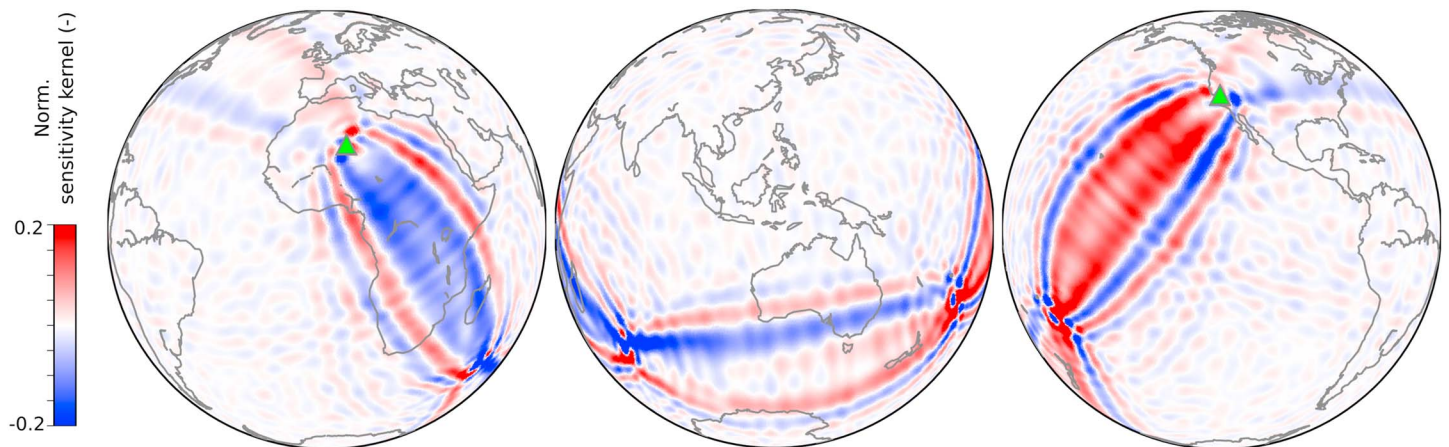


**Figure 4.** An example of the source sensitivity kernel associated with the measurement  $A_l$  for stations located in California and Algeria (marked by green triangles) and a period range of 120–330 s. For the measurement  $A_l$  and the chosen measurement windows  $w_+$ ,  $w_-$  centered on surface waves traveling with a group velocity of  $3.7 \frac{\text{km}}{\text{s}}$ , sensitivity is concentrated in the stationary-phase regions behind the stations. A particularity of the global scale and the long-period surface waves is that sensitivity refocuses at the antipodes of the stations. Furthermore, there is weak sensitivity also in between the stations due to multiple-orbit surface wave propagation.

3. On the global scale, sensitivity refocuses at the antipodes of the station locations. These are the locations where noise sources would produce a wavefield that focuses at the stations, thereby having a strong effect on the measurement.

After compiling the gradient from all sensitivity kernels and measurements, we apply a 95th percentile clipping and a Gaussian smoothing filter to the negative gradients before updating. This preconditioning is intended to avoid artifacts that would result from imperfect coverage. During the first three iterations, the standard deviation of the smoothing filter is set to 500 km and during subsequent iterations to 250 km. After each gradient is obtained, we conduct a line search for optimal step length using a subset of  $\approx 20\%$  of the observed data. Updates are performed using the conjugate gradient algorithm. We terminate the inversions once the remaining residual drops below the data error estimated in section 3.2.

## 4. Results

The hum source models resulting from the inversion are summarized in Figure 5. The models are normalized, because the asymmetry measurement is insensitive to a scaling of the absolute noise PSD. In the following, we will discuss these models, and present two synthetic inversions intended to assess resolution.

### 4.1. Inversion 1: North Hemisphere Winter

The stopping criterion was reached after six iterations. The mean misfit per observed cross correlation was reduced by 18% during the inversion. Compared to the data uncertainty, which was estimated at 0.3 for this seasonal stack, the mean remaining difference between observed and synthetic asymmetry of 0.31 is still sufficiently large to indicate that we did not overfit the data. In Figure 6, we show cross-correlation envelopes of observed and synthetic (starting and final) cross correlations for NH winter. In most cases, relative amplitudes of the final synthetics approach those of the observations. Several cross-correlation envelopes, for example, for station pairs G.CAN–G.TRIS and G.CAN–G.SCZ, show signals at short time lags. These may at least partly be due to coherently propagating surface waves from persistent sources located outside the stationary-phase region (Gaudot et al., 2016; Retailleau et al., 2017). However, our source model does not reproduce these features, which will be discussed in section 5.

Locations of dominant source PSD are found in the oceans. The most salient feature of the model is a rim of strong source PSD around the Pacific. It extends from the North American Pacific coast via the Al $\acute{e}$ utian arc, Kamtchatka, Japan, and Izu-Bonin to Fiji and Samoa. Additional strong sources appear in the North Atlantic extending southward from Greenland and westward from the European coast. The Gulf of Mexico also shows elevated source PSD. Finally, an elevated PSD level is visible across the central Pacific. Anticipating the results of the recovery tests and discussion, we suggest to pay less attention to features beside these ones that are the most prominent.

### 4.2. Inversion 2: South Hemisphere Winter

In the inversion for SH winter, we again iterated until the average misfit dropped below the estimated data uncertainty. We used the higher value of estimated data uncertainty of 0.3 for NH winter to be conservative. The final model was obtained after five iterations, yields a misfit reduction of 15%, and is shown in Figure 5. A model after a further six iterations is shown for comparison in Figure S3.

The model for SH winter shows mostly different patterns from NH winter. During SH winter, source PSD is clearly dominated by the South Hemisphere and distributed in several localized patches. The largest one is located off the Chilean coast. There is a chain of patches extending from the South Sandwich islands region toward the Indian Ocean, two south of Australia, one between Fiji and Samoa, and several in the larger Philippine Sea region. Similarities to the NH winter model are the strong excitation off the Chilean coast and the sources in the Philippine Sea and the Izu-Bonin region.

### 4.3. Synthetic Recovery Tests

The STS-1s network that we used here is irregularly distributed with 102 stations in the Northern and only 46 in the Southern Hemisphere. To estimate the resolution of our models, which we expect to be largely controlled by the receiver distribution, we set up two recovery tests with sources shaped as positive Gaussian anomalies on a source-free background (similar to Nishida & Fukao, 2007). We choose anomalies with standard deviations of 350, 500, and 1,000 km and locate them in shelf regions as well as pelagic regions of both hemispheres. The target models are shown in Figures 7 (first column) and 7 (third column).

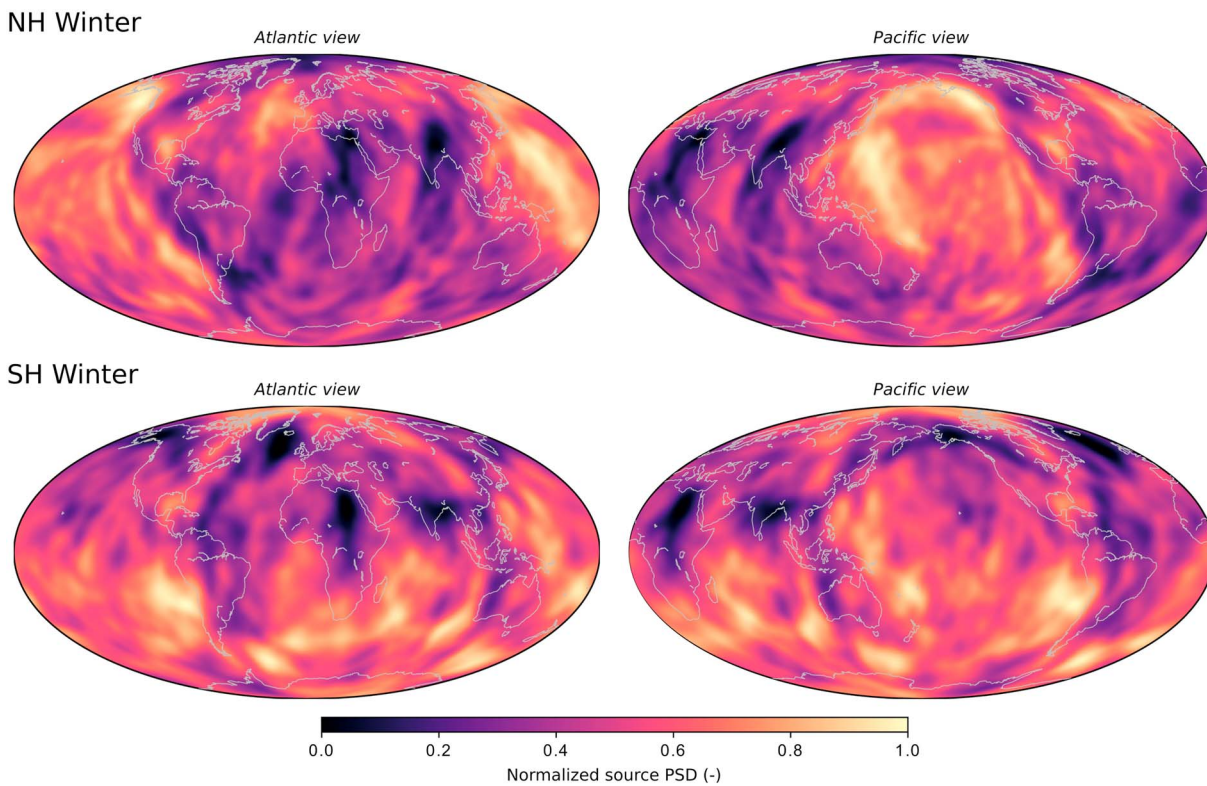


**Figure 5.** Results of the two seasonal inversions. The normalized source PSD model for (top row) NH winter and (bottom row) SH winter. The NH winter model was obtained after six iterations, the SH winter model after five iterations. The models show a clear seasonal variation of dominant source locations, with strong sources around the Pacific and in the North Atlantic during NH winter, and around the South Pacific and Southern Ocean in SH winter.

The target models are used to compute synthetic data, which then serve as input for the inversion. Since we are mainly interested in the influence of the array shape on the recovery, we did not add noise to the synthetic data. We run an inversion with four iterations for each recovery test. As the synthetic data are noise-free, we predefined this number of iterations to avoid an overly optimistic estimate of resolution. An intriguing aspect of the recovery tests is that although ambient sources are located in only few patches, the resulting synthetic cross correlations show very clear Rayleigh waves and hardly any spurious arrivals, as illustrated in Figure S4. The recovered models are shown in Figures 7 (second column) and 7 (fourth column). The first observation is that sources located far from most stations are resolved better. In test 2, source locations are recovered better

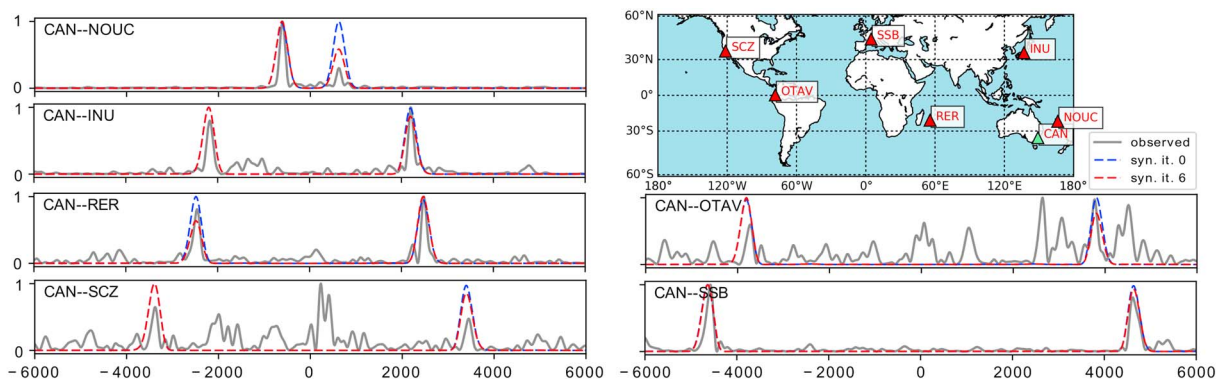


**Figure 6.** Normalized envelopes of observed correlations (gray solid line), synthetic correlations of the starting (blue dashed line), and final model (red dashed line) for NH winter. Station locations are shown on the map. For many observed cross correlations, the Rayleigh wave envelope emerges clearly. For certain station pairs, additional phases at low lags appear. Their observation at pairs of quiet stations indicates they are due to coherently propagating surface waves caused by strong persistent sources located outside of the stationary-phase region of the receiver pair. See Figure S2 for the remaining envelopes of cross correlations with respect to reference station G.CAN.

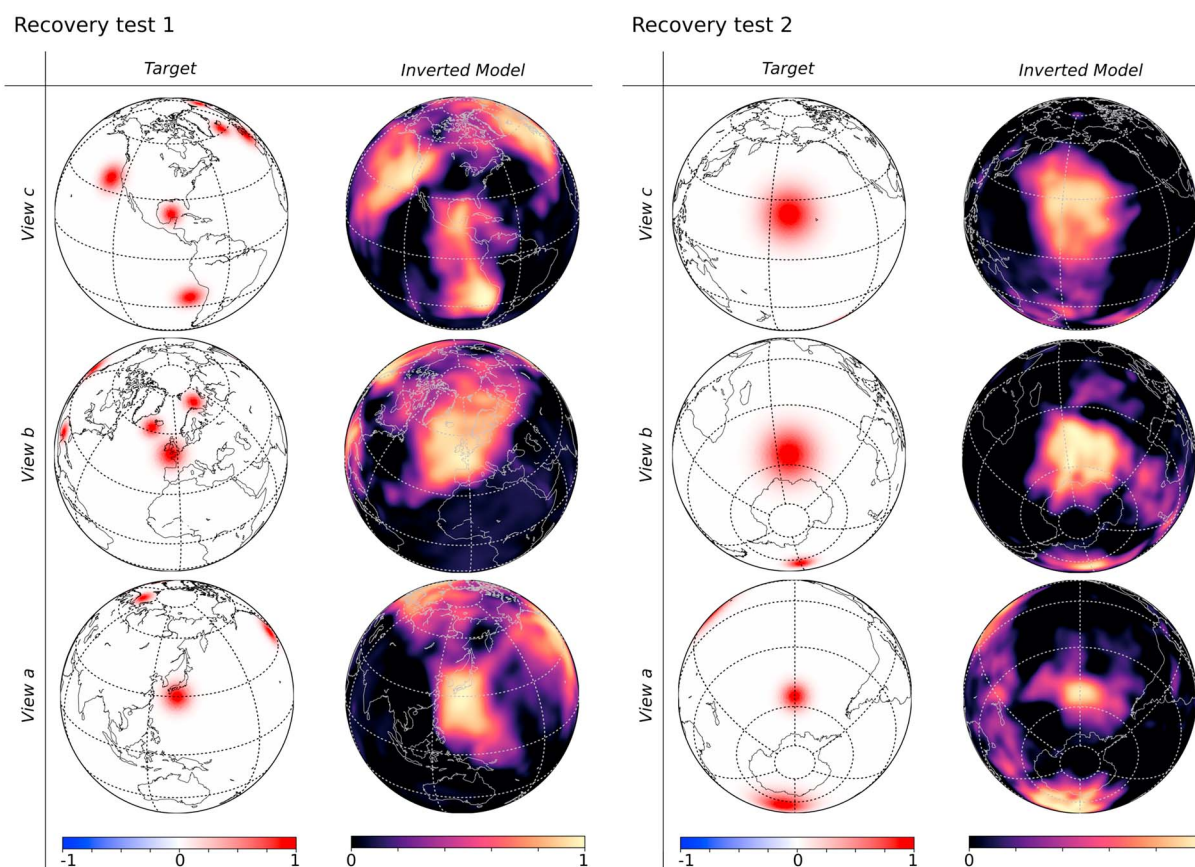


**Figure 7.** We performed two synthetic inversions to investigate the recovery of localized sources. (first and third columns) The target model of each test in three different perspectives, each focusing on a different source region. The target models were used to simulate synthetic data. We inverted the synthetic data performing four iterations, starting from a homogeneous initial source model. (second and fourth columns) The recovered models are shown.

than in test 1, although they are located in the central Pacific and the Southern Ocean, far from most stations of the array. While this may appear counterintuitive, it is a direct consequence of sensitivity being concentrated behind and not between station pairs, as shown in Figure 4. The second observation is that resolution depends on location and is on the order of 1,000 km. Finally, we note that smearing from a near-coastal source to the ocean appears more pronounced than from a pelagic source toward the coastline. The resolution tests provide us with the insight needed to discuss our results in the context of the existing literature on hum sources.

## 5. Discussion

### 5.1. Interpretation of the Hum Source Models

Our hum source models are in good qualitative agreement with previous studies (e.g., Bromirski & Gerstoft, 2009; Nishida & Fukao, 2007; Rhie & Romanowicz, 2004, 2006; Traer et al., 2012). The seasonal excitation pattern is consistent with the ones reported by Rhie and Romanowicz (2004), Nishida and Fukao (2007), and Traer et al. (2012). While we use a longer observation period, our model captures the strongest source locations reported by Rhie & Romanowicz (2004, 2006) and Bromirski and Gerstoft (2009) during the relevant seasons, namely a location close to the South Sandwich Islands during SH winter, the European Atlantic coast during NH winter, and the Pacific Northwest coast where two separate events in 2000 and 2006 have been reported. Detection by the 10 year average model indicates that these locations all contribute persistently during the relevant season to the excitation of hum.

We located a number of additional sources in the Southern Hemisphere, during both NH and SH winter. In NH winter, we find a rim of high source PSD around the Pacific that extends from California to Kamtchatka—similar to locations identified during 2010/2011 by Traer et al. (2012)—and from the Philippine Sea toward Fiji and Samoa. In SH winter, source locations are confined to localized patches in the Southern Ocean, southwest of New Zealand, southwest of Australia, southeast of Madagascar, as well as to the south

and southwest of the South African coast. We again find high source PSD in the Philippine Sea, as well as close to Fiji, during SH winter. Based on the recovery tests, we place some confidence in the locations of the strongest peaks of source PSD, without interpreting the outlines or shapes of the features surrounding them.

#### **5.1.1. Detailed Comparison With Previous Longer-Term Models and Ocean Infragravity Wave Models**

Dominant source regions are consistent with results from previous longer-term studies (e.g., Nishida & Fukao, 2007; Traer et al., 2012). Our broad pattern of source locations agrees with the results by Nishida and Fukao (2007).

However, the features of our models are more localized. In particular, our NH winter model shows a sharper rim around and a lower level of excitation within the central Pacific. In contrast, the model of Nishida and Fukao (2007) shows high effective pressure throughout the Northern Central Pacific. We attribute the shorter-scale features of our model to the larger number of stations, the shorter periods (100–300 s versus 100–500 s in Nishida and Fukao, 2007), to the iterative improvement during which smaller-scale features emerge and to the parameterization of the source model on a fine grid. Based on recovery tests in both studies, we suggest that our model improves upon the resolution insofar as it does not tend to introduce spurious maxima at some distance from the target source location. This may be due to the different measurements used: While the amplitude measurement of Nishida and Fukao (2007) is primarily sensitive to even-degree spherical harmonics, our measurement has antisymmetric sensitivity kernels (see Figure 4). The hum excitation features stretching west and south from the American West coast may be explained by smearing of sources located close to the Californian coast, according to our recovery test. This prevents us from drawing conclusions on the contribution of pelagic sources in this region.

Comparing to the source locations in Traer et al. (2012), our NH winter model equally shows high source PSD along the North Pacific coast, in the North Atlantic between Greenland and Spain, and along the Chilean coast. In SH winter, our model also shows a source region off the Chilean coast and a source region close to South Sandwich Islands. We observe additional source locations in accord with Nishida and Fukao (2007). There are two possible explanations why they are not observed by Traer et al. (2012). The first is the shorter duration covered by their data set of only 1 year. The second is that the shape of the two arrays used in their study may be unfavorable for waves incident along an east-west axis, which could explain that strong sources in the West Pacific were not observed.

Ardhuin et al. (2014) developed an empirical model of ocean infragravity wave height. A global map averaged over North and South Hemisphere winter season is shown in their Figure 6. Bearing in mind that the observation times are different and that hum sources result from the interaction of infragravity waves with bathymetry, rather than infragravity waves alone, the comparison yields two similarities: The first is a consistent seasonal hemispheric shift of both infragravity wave heights and strong hum sources, the second is the strong excitation of hum at the west coasts of the Americas and Europe during North Hemisphere winter. This is consistent with west coasts experiencing particularly high infragravity waves during that season.

#### **5.1.2. Impact of Network Geometry and Smoothing**

To exclude that prominent source areas are due to a focusing of sensitivity, we analyzed the shape of the network sensitivity. For this, we computed the finite-frequency equivalent of ray coverage by summing the absolute values of all sensitivity kernels from equation 20, with data residuals for all station pairs set to 1. The resulting sensitivity map, similar to those used in waveform inversion (e.g., Tape et al., 2010), is shown in Figure S5 of the supporting information. It contains no indication that spots of high sensitivity systematically coincide with strong features of our models. Furthermore, the sensitivity map emphasizes that sensitivity and resolution are both limited north of 30°N. Importantly, they also demonstrate that the locations of many station antipodes lead to small-scale, high-sensitivity locations in the Southern Ocean (cf. Figure 4).

We further compared our preferred SH winter model in Figure 5 to one with a shorter smoothing length scale of  $\sigma = 250$  km, shown in Figure S6. Although reducing the smoothing changes the details of the discussed features, their locations and peak values remain stable. From this we conclude that our results are reasonably robust with respect to network geometry and smoothing.

#### **5.1.3. Cumulative Effect of Earthquakes**

In the time interval spanned by our continuous data set, more than 5,500 earthquakes with magnitude  $>5.5$  occurred, according to the USGS catalog (<https://earthquake.usgs.gov/earthquakes/search/>). Suda et al. (1998) show that these contribute to the normal-mode peaks of the hum, although they are not sufficient to explain it. While the largest events occur infrequently enough to be outweighed during stacking

by persistent hum signals, thanks to our normalization procedure, less strong events that frequently occur in similar regions may have contributed to our models. It was shown recently that various normalization procedures are insufficient to remove their signature, at least from data of shorter periods (Seydoux et al., 2016; Yanovskaya et al., 2016). Most features of our models shift seasonally, indicating environmental excitation. There are, however, three regions where hum excitation is strong in both seasons; off the Chilean coast, the Izu-Ogasawara and Mariana region, and the Fiji basin (see Figure S7 in the supporting information).

Three arguments suggest that also these parts of the model are dominated by ambient signals. First, our results are consistent with Nishida and Fukao (2007), who used a wholly different procedure of earthquake removal by data selection. Second, several areas of strong seismicity do not appear in our model, among them the location of the 2004 Sumatra-Andaman event with a large number of aftershocks. Third, a hum source off the coast of Chile is also observed by Traer et al. (2012), who additionally show that its temporal evolution correlates with ocean wave activity during SH winter.

#### 5.1.4. Hypotheses for Hum Sources

Based on these considerations, we propose the following interpretations of our models. Taking into account limited resolution and the difficulty to exclude contributions of small earthquakes with absolute certainty, these should be regarded as working hypotheses.

Bromirski and Gerstoft (2009), Traer et al. (2012), and Traer and Gerstoft (2014) argue for coastal excitation of the hum in shallow water, while Arduin et al. (2015) has demonstrated a mechanism that requires hum to be excited at shelf breaks. Our results can be plausibly explained by either mechanism. Our models clearly support the near-coastal excitation areas previously reported, without being able to distinguish if these are linked to shallow water or the sloping shelf, due to insufficient resolution and smearing from the coast toward the open ocean, for example, off the Chilean coast. In addition we find a number of features during SH winter for which excitation on continental coastlines is not plausible. In particular, these are the source located close to the South Sandwich Islands, the source near Fiji, and the sources in the Marianas and Izu-Ogasawara region. They may be linked to regions of high and complex bathymetry, including islands. The strong hum PSD features observed in our models are comparatively narrow, while Gaussian-shaped sources in the recovery test are laterally smeared. This indicates that hum sources may in fact be more localized than those in the target models of the recovery test, that is, to within around 100 km. An observation that further supports this interpretation is the appearance of arrivals near zero lag on cross correlations at several quiet stations (Figure 6). If the sources were more extended, their signals would cancel due to the oscillating nature of the sensitivity kernel outside the stationary-phase region (Figure 4). This is also reflected in our observation that the synthetic models of the recovery tests show no such spurious arrivals. If our interpretation holds, it corroborates the finding by Nishida and Kobayashi (1999), based on statistical features of the hum, that hum sources must have a spatial correlation length of less than 600 km. It is furthermore consistent with the estimate of Tanimoto (2005) that infragravity waves over small areas on the order of 100 by 100 km are sufficient to account for the observed seismic signal levels.

## 5.2. Discussion of the Method

The applicability of our method rests on the use of precomputed wavefields and various assumptions that we will briefly discuss in the following paragraphs.

### 5.2.1. Effects of Parameterization

We used a fixed, spatially uniform spectral basis function between  $\sim 125$ – $330$  s. Hence, our model cannot resolve differences in the shape of the spectrum of different hum sources. A direction of future research is therefore to extend our approach to a sequential inversion for different frequency bands. The synthetic study by Sager et al. (2017) indicates, however, that joint frequency-dependent noise source inversion is difficult to conduct because measurements with sufficient sensitivity to spectral content of the cross correlation show large trade-offs with unmodeled Earth structure.

For the spatial parameterization of precomputed wavefields and source distributions, we used a regular grid with  $\sim 10$  grid points per shortest wavelength. This choice naturally influences the inversion results. The gridded parameterization allows us to retrieve more detail than the low-order spherical harmonics used by Nishida and Fukao (2007). It is, however, also more prone to overfitting, which we have sought to avoid by stopping the inversions before the average misfit dropped below the estimated data uncertainty. Gridded parameterization appears as an opportune choice, because the extent or correlation length

of particular sources is poorly known, and sources may be confined to narrow areas such as shelf breaks (Ardhuin et al., 2015).

### 5.2.2. Effects of Processing, Synthetics Duration, and Attenuation on Amplitudes

Any study on long-range ambient cross correlations employs some form of data processing (e.g., Boué et al., 2014; Nishida, 2013; Stehly et al., 2006). A notable exception is found in Nishida and Fukao (2007), who used an elaborate rejection filter instead. Here we have used normalization by trace energy, which is expected to alter cross-correlation amplitudes. Our forward model does not include such a normalization. While the asymmetry measurement  $A$ , is entirely insensitive to absolute amplitudes, these discrepancies have implications for the misfit gradient with respect to the source PSD. Conceptually, we expect that sources located at some distance from stations and station antipodes may be downweighted compared to sources close to the stations and their antipodes by the inversion due to processing effects. In the normalized cross correlations, perfectly coherent signals attain a cross-correlation value of 1 regardless of their absolute amplitudes, whereas in the case of nonnormalized cross correlations, less attenuated local signals can dominate. We expect no significant effect on our current models, because we should otherwise see a higher correlation of the final models with network sensitivity (see Figure S5 in the supporting information). However, for further refinement of the method, all processing should be taken into account either by removing it as far as possible (Nishida & Fukao, 2007) or by the approach of Fichtner et al. (2017).

The attenuation model, taken from PREM (Dziewoński & Anderson, 1981), also affects amplitudes and sensitivity (e.g., Ermert et al., 2016). Since attenuation of long-period surface waves is generally weak, we expect its lateral variations to have only a minor effect. It may, however, be significant in regional studies. It may be possible to make a virtue of necessity and extract attenuation estimates from long-range ambient correlations, similar to Prieto and Beroza (2008). The ambient source inversion method presented here is a key tool to do so (Stehly & Boué, 2017). However, the large amplitude uncertainty of our current data set prevents its immediate use for attenuation studies.

Finally, the duration of the synthetic Green's functions has an influence on the sensitivity kernels (see Figure S1). Schimmel et al. (2011) showed that minor- and major-arc Rayleigh waves can be observed to propagate coherently between station pairs. Hence, the typical propagation distance of hum must be at least one orbit and is possibly longer. We took a conservative approach and allowed for several multiple orbits.

### 5.2.3. Assumptions About Hum Sources

We have limited the modeling here to vertical point sources and the  $zz$  component of the source PSD. Through the precomputation of wave fields also for horizontal sources, all other components can theoretically be taken into account. This would increase the number of model parameters by nearly an order of magnitude that could not be matched by additional high-quality data on all components of the noise correlation tensor. Hence, at least on the global scale, such an extension is currently out of reach.

In equation (4), we have assumed that sources are spatially uncorrelated. Although this assumption is commonly used, its influence on the resulting forward model is not well known. Only some theoretical considerations have been presented by Godin (2009).

The precomputed wavefield approach can be extended to relax this. There are two possible ways to do this. The first is to model noise time series by the approach of van Driel et al. (2015), but using a 3-D precomputed, rather than a spherically symmetric Green's function database and introducing a finite correlation length into the random-phase source field. This approach appears well suited for exploratory forward models, in particular, to simulate spatially varying temporal and spatial source spectra. The second approach is to introduce a band-limited spatial spectrum with a predefined correlation length  $L$  into equation (3). Instead of equation (6), one would then evaluate

$$C_{ij}(\mathbf{x}_1, \mathbf{x}_2, \tau) = \int_{\partial\oplus} G_{ni}(\xi, \mathbf{x}_1, -t) * \left[ \int_{\Delta\xi=-L}^L G_{mj}(\xi + \Delta\xi, \mathbf{x}_2, t) * N_n(\xi, -t) * N_m(\xi + \Delta\xi, t) d\Delta\xi \right] (\tau) d\xi. \quad (28)$$

In this case, the cross-correlation function of sources  $N_n(\xi, -t)$  and  $N_m(\xi + \Delta\xi, t)$  would have to be evaluated, while our current assumption of a white spatial spectrum makes it sufficient to use the source autocorrelation. One might also assume some functional form of the cross correlation between noise sources, which would allow us to evaluate the cross correlation as before, but with a distance-dependent term replacing the delta function in equation (3). Since there are hardly any observational constraints on the spatial spectrum

of the noise sources (an upper limit of the correlation length  $L$  has been estimated by Nishida & Kobayashi, 1999), it appears arbitrary to include it in the cross-correlation modeling at this point.

#### 5.2.4. Usability for Cross-Correlation Waveform Inversion

To evaluate the viability of the source inversion for a future global tomography based on cross-correlation waveforms, we determined the phase misfit of observed cross correlations with starting and final synthetics. We found a misfit reduction of negligible magnitude ( $\sim 1\%$ ). This is not surprising, as we are evaluating the phases of stationary-phase Rayleigh waves, which were already reasonably well fit by our starting model (Figure 3). Phase shifts due to smooth variations in source distribution are expected to be small (Froment et al., 2010), in particular, due to the global propagation of long-period Rayleigh waves. Importantly, however, the application shown here demonstrates that it is feasible to obtain models of noise source distribution which may be used for noise cross-correlation waveform inversion and which should provide a more realistic illumination of the structure. With the precomputed wavefield approach, the method can more or less seamlessly be translated to the regional scale.

Since we normalized cross correlations by trace energies, modeled and observed absolute amplitudes are not trivially related. For tomographic inversion, it is therefore necessary to use an amplitude-independent misfit, such as the time frequency-phase misfit, in keeping with common tomographic practice (e.g., Fichtner, 2010). Alternatives would be the generalized interferometry approach of Fichtner et al. (2017), or the computation of cross correlations without normalization, which can again only be achieved through careful data selection.

Finally, we did not explicitly account for the effect of local uncorrelated noise in our forward model. The effect of local noise on cross-correlation amplitudes and its resulting influence on our nonlinear measurement would require further detailed analysis that is presently out of scope. Therefore, we have limited our treatment of noise to the estimation of a measurement uncertainty in order to avoid fitting effects of local noise.

#### 5.2.5. Can We Improve the Resolution of Hum Source Inversions?

Resolution of the inversion we have presented here is not least limited by the long wavelengths of the Earth's hum. Future studies should target the higher-frequency end of the Earth's hum to increase resolution. Based on this study, we suggest two additional strategies to improve it and provide better constraints for physical excitation models. First, station coverage may be increased. Although arguably only quiet stations provide long-range cross correlations of sufficient quality at hum periods, there is a number of stations operating high gain very broadband vault and borehole seismometers that are currently not included in our data set.

Second, one may utilize the apparent high velocity spurious arrivals described earlier. The sensitivity regions of such arrivals correspond approximately to narrow hyperbolas between the receivers. Accounting for them during inversion adds a large amount of sensitivity to short-wavelength features (e.g., Retailleau et al., 2017). Including them into the inversion procedure can be achieved by using measurements targeted at the amplitudes of the whole cross correlation waveform, such as the envelope misfit by Sadeghisorkhani et al. (2016). Our method would account for both body and surface wave arrivals in the waveform envelope. A reduction of the amplitude uncertainty of the cross correlations would be necessary before using the envelope measurement.

## 6. Conclusions

With the aim to work toward ambient noise cross-correlation waveform inversion, as well as to provide new observational constraints on ambient noise excitation, we developed and applied a novel inversion method for the sources of ambient noise. It accounts for both finite frequency wave propagation and laterally heterogeneous Earth structure.

We conclude that our method is effective at locating ambient seismic sources and improving the fit to the relative cross-correlation signal energies. It provides global hum source models that are physically reasonable and consistent with previous studies, while offering a more general and slightly more detailed result than many of them. It is the first application of this inversion technique to an observed cross-correlation data set, after a series of theoretical papers (e.g., Fichtner, 2014, 2015; Hanasoge, 2013b; Tromp et al., 2010) and the sensitivity study of Basini et al. (2013). It constitutes a step toward the application of noise cross-correlation waveform tomography as anticipated by the theoretical and synthetic studies of Hanasoge (2013a) and Sager et al. (2017).

Our hum source models for North and South Hemisphere winter show narrowly concentrated areas of high excitation with seasonally shifting patterns. Source locations off the coast of Chile, close to Fiji and in the Marianas region show little seasonal variation. Based on comparisons to the results of Nishida and Fukao (2007) and Traer et al. (2012), we suggest that these are caused by ambient rather than earthquake activity. Our results do not permit a direct distinction between excitation in shallow water and along shelf breaks (Arduin et al., 2015; Traer & Gerstoft, 2014) due to limited resolution. We find source locations which are more likely linked to islands and regions of complex bathymetry, than to continental coastlines. A remarkable feature of the long-period cross correlations is the occurrence of signals from sources outside the stationary-phase region. These indicate frequently recurring, narrowly localized source spots for the seismic hum and merit further investigation.

#### Acknowledgments

We thank two anonymous reviewers for their constructive review of the manuscript. We gratefully acknowledge insightful comments from and discussions with Laurent Stehly and Kiwamu Nishida. We also acknowledge discussions enabled by, and support received from, COST Action ES 1401: TIDES. This research was crucially supported by the Swiss National Supercomputing Center (CSCS) and the Platform for Advanced Scientific Computing (PASC) in the form of projects GeoScale, ch1 and s741; by Schweizerischer Nationalfonds zur Förderung der Wissenschaftlichen Forschung (SNF) under grant 200021\_149143; and by Nederlandse Organisatie voor Wetenschappelijk Onderzoek under VIDI grant 864.11.008. Data used for the preparation of the results are fully public and available at IRIS (see below). The processing code used to calculate noise cross correlations is available at [https://github.com/lermert/ants\\_2](https://github.com/lermert/ants_2). The code for obtaining synthetic cross correlations and source sensitivity kernels is available at <https://github.com/lermert/noisi>. The global cross-correlation data set is available from the authors on request. This research benefitted from metadata provided by the Geoscope network (<http://geoscope.ipgp.fr/index.php/en/>). The facilities of IRIS Data Services, and specifically the IRIS Data Management Center, were used for access to waveforms and related metadata. IRIS Data Services are funded through the Seismological Facilities for the Advancement of Geoscience and EarthScope (SAGE) Proposal of the National Science Foundation under Cooperative agreement EAR-126168. DOIs of the networks used, wherever available, are listed as follows: <https://doi.org/10.14470/TR560404>; <https://doi.org/10.7932/BDSN>; <https://doi.org/10.7914/SN/IC>; <https://doi.org/10.7914/SN/II>; <https://doi.org/10.7914/SN/IU>; [www.fdsn.org/networks/detail/CI/](http://www.fdsn.org/networks/detail/CI/); [www.fdsn.org/networks/detail/G/](http://www.fdsn.org/networks/detail/G/); [www.fdsn.org/networks/detail/GB/](http://www.fdsn.org/networks/detail/GB/); [www.fdsn.org/networks/detail/MN/](http://www.fdsn.org/networks/detail/MN/); and [www.fdsn.org/networks/detail/MS/](http://www.fdsn.org/networks/detail/MS/).

#### Appendix A: Link to the Kernel Formulation of Stehly and Boué (2017)

It may be illustrative to link our derivation of source sensitivity kernels to the one presented by Stehly and Boué (2017). They suggest an approach to the inversion for noise sources that use a simple misfit function, is intuitive, and connects naturally to approaches using more elaborate misfit functions such as the ones introduced above. Here we outline this connection.

In their description of the source kernel, they explain that the measurement is taken through comparison of two cross correlations by taking the difference of their amplitudes at the lag time  $\tau_{\text{peak}}$  when the largest peak occurs. Their measurement can thus be described as

$$C_p = \int C_{ij}(\tau) \cdot \delta(\tau - \tau_{\text{peak}}) d\tau, \quad (\text{A1})$$

and the  $L_2$  misfit function as

$$\chi = \frac{1}{2} [C_p - C_p^o]^2. \quad (\text{A2})$$

The derivative of this misfit function with respect to the model  $C_{ij}$  is

$$\nabla_c \chi^o = \int [C_p - C_p^o] \cdot \delta(\tau - \tau_{\text{peak}}) d\tau, \quad (\text{A3})$$

and consequently, the misfit variation due to a change of source PSD becomes according to equations (10) and (11)

$$\begin{aligned} \nabla_s \chi \delta S &= [C_p - C_p^o] \cdot \int \int_{\partial \oplus} \delta(\tau - \tau_{\text{peak}}) \cdot (G_{jm}(\mathbf{x}, \xi, t) * G_{in}(\mathbf{x}_1, \xi, -t) * \delta S(\xi, t))(\tau) d\xi d\tau \\ &= [C_p - C_p^o] \cdot \int_{\partial \oplus} (G_{jm}(\mathbf{x}, \xi, t) * G_{in}(\mathbf{x}_1, \xi, -t) * \delta S(\xi, t))(\tau_{\text{peak}}) d\xi, \end{aligned}$$

leaving us with a space-dependent sensitivity kernel that is exactly the evaluation of the synthetic cross correlation itself at  $\tau_{\text{peak}}$ , scaled by the difference between peak amplitudes as described by Stehly and Boué (2017). Returning to other misfit functions simply requires replacing equations A2 and A3 by the corresponding expressions for  $\chi$  and  $\nabla_c \chi$ .

#### References

- Afanasiev, M., Peter, D., Sager, K., Simutè, S., Ermert, L., Krischer, L., & Fichtner, A. (2016). Foundations for a multiscale collaborative earth model. *Geophysical Journal International*, 204(1), 39–58. <https://doi.org/10.1093/gji/ggv439>
- Aki, K., & Richards, P. (2002). *Quantitative seismology*. Sausalito, CA: University Science Books.
- Anthony, R. E., Aster, R. C., & McGrath, D. (2017). Links between atmosphere, ocean, and cryosphere from two decades of microseism observations on the Antarctic Peninsula. *Journal of Geophysical Research: Earth Surface*, 122, 153–166. <https://doi.org/10.1002/2016JF004098>
- Arduin, F., Gualtieri, L., & Stutzmann, E. (2015). How ocean waves rock the Earth: Two mechanisms explain microseisms with periods 3 to 300 s. *Geophysical Research Letters*, 42, 765–772. <https://doi.org/10.1002/2014GL062782>
- Arduin, F., Rawat, A., & Aucan, J. (2014). A numerical model for free infragravity waves: Definition and validation at regional and global scales. *Ocean Modelling*, 77, 20–32. <https://doi.org/10.1016/j.ocemod.2014.02.006>
- Aster, R. C., McNamara, D. E., & Bromirski, P. D. (2010). Global trends in extremal microseism intensity. *Geophysical Research Letters*, 37, L14303. <https://doi.org/10.1029/2010GL043472>
- Basini, P., Nissen-Meyer, T., Boschi, L., Casarotti, E., Verbeke, J., Schenk, O., & Giardini, D. (2013). The influence of nonuniform ambient noise on crustal tomography in Europe. *Geochemistry, Geophysics, Geosystems*, 14, 1471–1492. <https://doi.org/10.1002/ggge.20081>
- Bassin, C., Laske, G., & Masters, G. (2000). The current limits of resolution for surface wave tomography in North America. *Eos, Transactions American Geophysical Union*, 81, F897.

- Behr, Y., Townend, J., Bannister, S., & Savage, M. K. (2010). Shear velocity structure of the Northland Peninsula, New Zealand, inferred from ambient noise correlations. *Journal of Geophysical Research*, *115*, B05309. <https://doi.org/10.1029/2009JB006737>
- Bensen, G. D., Ritzwoller, M. H., Barmin, M. P., Levshin, A. L., Lin, F., Moschetti, M. P., ... Yang, Y. (2007). Processing seismic ambient noise data to obtain reliable broad-band surface wave dispersion measurements. *Geophysical Journal International*, *169*, 1239–1260.
- Beyreuther, M., Barsch, R., Krischer, L., Megies, T., Behr, Y., & Wassermann, J. (2010). ObsPy: A python toolbox for seismology. *Seismological Research Letters*, *81*(3), 530–533. <https://doi.org/10.1785/gssrl.81.3.530>
- Boschi, L., & Weemstra, C. (2015). Stationary-phase integrals in the cross correlation of ambient noise. *Reviews of Geophysics*, *53*, 411–451. <https://doi.org/10.1002/2014RG000455>
- Boué, P., Poli, P., Campillo, M., & Roux, P. (2014). Reverberations, coda waves and ambient noise: Correlations at the global scale and retrieval of the deep phases. *Earth and Planetary Science Letters*, *391*, 137–145. <https://doi.org/10.1016/j.epsl.2014.01.047>
- Bowden, D. C., Tsai, V. C., & Lin, F. C. (2015). Site amplification, attenuation, and scattering from noise correlation amplitudes across a dense array in Long Beach, CA. *Geophysical Research Letters*, *42*, 1360–1367. <https://doi.org/10.1002/2014GL026662>
- Bozdağ, E., Peter, D., Lefebvre, M., Komatitsch, D., Tromp, J., Hill, J., ... Pugmire, D. (2016). Global adjoint tomography: First-generation model. *Geophysical Journal International*, *207*(3), 1739–1766. <https://doi.org/10.1093/gji/ggw356>
- Bromirski, P. D. (2001). Vibrations from the 'Perfect Storm'. *Geochemistry, Geophysics, Geosystems*, *2*(7), 1030. <https://doi.org/10.1029/2000GC000119>
- Bromirski, P. D., & Duennebier, F. K. (2002). The near-coastal microseism spectrum: Spatial and temporal wave climate relationships. *Journal of Geophysical Research*, *107*(B8), 2166. <https://doi.org/10.1029/2001JB000265>
- Bromirski, P. D., & Gerstoft, P. (2009). Dominant source regions of the Earth's "hum" are coastal. *Geophysical Research Letters*, *36*, L13303. <https://doi.org/10.1029/2009GL038903>
- Brzak, K., Gu, Y. J., Ökeler, A., Steckler, M., & Lerner-Lam, A. (2009). Migration imaging and forward modeling of microseismic noise sources near southern Italy. *Geochemistry, Geophysics, Geosystems*, *10*, Q01012. <https://doi.org/10.1029/2008GC002234>
- Chen, M., Huang, H., Yao, H., van der Hilst, R., & Niu, F. (2014). Low wave speed zones in the crust beneath SE Tibet revealed by ambient noise adjoint tomography. *Geophysical Research Letters*, *41*, 334–340. <https://doi.org/10.1002/2013GL058476>
- Chen, P., Zhao, L., & Jordan, T. H. (2007). Full 3D tomography for the crustal structure of the Los Angeles region. *Bulletin of the Seismological Society of America*, *97*, 1094–1120.
- Chevrot, S., Sylvander, M., Benahmed, S., Ponsolles, C., Lefèvre, J. M., & Paradis, D. (2007). Source locations of secondary microseisms in western Europe: Evidence for both coastal and pelagic sources. *Journal of Geophysical Research*, *112*, B11301. <https://doi.org/10.1029/2007JB005059>
- Cupillard, P., & Capdeville, Y. (2010). On the amplitude of surface waves obtained by noise correlation and the capability to recover the attenuation: A numerical approach. *Geophysical Journal International*, *181*(3), 1687–1700.
- Dales, P., Audet, P., Olivier, G., & Mercier, J.-P. (2017). Interferometric methods for spatio-temporal seismic monitoring in underground mines. *Geophysical Journal International*, *210*, 731–742. <https://doi.org/10.1093/gji/ggx189>
- de Ridder, S. A. L., Biondi, B. L., & Clapp, R. G. (2014). Time-lapse seismic noise correlation tomography at Valhall. *Geophysical Research Letters*, *41*, 6116–6122. <https://doi.org/10.1002/2014GL061156>
- Delaney, E., Ermert, L., Sager, K., Kritski, A., Bussat, S., & Fichtner, A. (2017). Removal of traveltimes errors in time-lapse passive seismic monitoring induced by non-stationary noise sources. *Geophysics*, *82*(4), K557–K570. <https://doi.org/10.1190/geo2016-0330.1>
- Denolle, M. A., Dunham, E. M., Prieto, G. A., & Beroza, G. C. (2013). Ground motion prediction of realistic earthquake sources using the ambient seismic field. *Journal of Geophysical Research: Solid Earth*, *118*, 2102–2118. <https://doi.org/10.1029/2012JB009603>
- Donne, S., Nicolau, M., Bean, C., & O'Neill, M. (2014). Wave height quantification using land based seismic data with grammatical evolution. In *2014 IEEE Congress on Evolutionary Computation (CEC)* (pp. 2909–2916). Beijing, China: IEEE.
- Dziewoński, A. M., & Anderson, D. L. (1981). Preliminary reference Earth model. *Physics of the Earth and Planetary Interiors*, *25*, 297–356.
- Ebeling, C. W., & Stein, S. (2011). Seismological identification and characterization of a large hurricane. *Bulletin of the Seismological Society of America*, *101*(1), 399–403. <https://doi.org/10.1785/0120100175>
- Ekström, G. (2001). Time domain analysis of Earth's long-period background seismic radiation. *Journal of Geophysical Research*, *106*(B11), 26,483–26,493. <https://doi.org/10.1029/2000JB000086>
- Ermert, L., Villaseñor, A., & Fichtner, A. (2016). Cross-correlation imaging of ambient noise sources. *Geophysical Journal International*, *204*(1), 347–364.
- Fang, H., Yao, H., Zhang, H., Huang, Y.-C., & van der Hilst, R. D. (2015). Direct inversion of surface wave dispersion for three-dimensional shallow crustal structure based on ray tracing: Methodology and application. *Geophysical Journal International*, *201*(3), 1251–1263. <https://doi.org/10.1093/gji/ggv080>
- Fichtner, A. (2010). *Full seismic waveform modelling and inversion*. Heidelberg: Springer.
- Fichtner, A. (2014). Source and processing effects on noise correlations. *Geophysical Journal International*, *197*, 1527–1531.
- Fichtner, A. (2015). Source-structure trade-offs in ambient noise correlations. *Geophysical Journal International*, *202*(1), 678–694.
- Fichtner, A., Kennett, B. L. N., Igel, H., & Bunge, H.-P. (2009). Full seismic waveform tomography for upper-mantle structure in the Australasian region using adjoint methods. *Geophysical Journal International*, *179*(3), 1703–1725. <https://doi.org/10.1111/j.1365-246X.2009.04368.x>
- Fichtner, A., Stehly, L., Ermert, L., & Boehm, C. (2017). Generalized interferometry I: Theory for interstation correlations. *Geophysical Journal International*, *208*(2), 603–638. <https://doi.org/10.1093/gji/ggw420>
- Froment, B., Campillo, M., Roux, P., Gouédard, P., Verdel, A., & Weaver, R. L. (2010). Estimation of the effect of nonisotropically distributed energy on the apparent arrival time in correlations. *Geophysics*, *75*, SA85–SA93.
- Fukao, Y., Nishida, K., & Kobayashi, N. (2010). Seafloor topography, ocean infragravity waves, and background love and Rayleigh waves. *Journal of Geophysical Research*, *115*, B04302. <https://doi.org/10.1029/2009JB006678>
- Gal, M., Reading, A. M., Ellingsen, S. P., Gualtieri, L., Koper, K. D., Burlacu, R., ... Hemer, M. A. (2015). The frequency dependence and locations of short-period microseisms generated in the Southern Ocean and West Pacific. *Journal of Geophysical Research: Solid Earth*, *120*, 5764–5781. <https://doi.org/10.1002/2015JB012210>
- Gaudot, I., Beucler, E., Mocquet, A., Schimmel, M., & Le Feuvre, M. (2016). Statistical redundancy of instantaneous phases: Theory and application to the seismic ambient wavefield. *Geophysical Journal International*, *204*(2), 1159–1163. <https://doi.org/10.1093/gji/ggv501>
- Gerstoft, P., & Bromirski, P. D. (2016). "Weather bomb" induced seismic signals. *Science*, *353*(6302), 869–870. <https://doi.org/10.1126/science.aag1616>
- Gerstoft, P., & Tanimoto, T. (2007). A year of microseisms in southern California. *Geophysical Research Letters*, *34*, L20304. <https://doi.org/10.1029/2007GL031091>
- Godin, O. A. (2009). Emergence of deterministic Green's functions from noise generated by finite random sources. *Physical Review E*, *80*(6), 66605.

- Gokhberg, A., & Fichtner, A. (2016). Full-waveform inversion on heterogeneous HPC systems. *Computers & Geosciences*, *89*, 260–268. <https://doi.org/10.1016/j.cageo.2015.12.013>
- Gouédard, P., Roux, P., Campillo, M., & Verdel, A. (2008). Convergence of the two-point correlation function toward the Green's function in the context of a seismic-prospecting data set. *Geophysics*, *73*(6), V47–V53. <https://doi.org/10.1190/1.2985822>
- Green, R. G., Priestley, K. F., & White, R. S. (2017). Ambient noise tomography reveals upper crustal structure of Icelandic rifts. *Earth and Planetary Science Letters*, *466*, 20–31. <https://doi.org/10.1016/j.epsl.2017.02.039>
- Gualtieri, L., Stutzmann, E., Capdeville, Y., Farra, V., Mangeney, A., & Morelli, A. (2015). On the shaping factors of the secondary microseismic wavefield. *Journal of Geophysical Research: Solid Earth*, *120*, 6241–6262. <https://doi.org/10.1002/2015JB012157>
- Halliday, D., & Curtis, A. (2008). Seismic interferometry, surface waves and source distribution. *Geophysical Journal International*, *175*, 1067–1087.
- Hanasoge, S. M. (2013a). Measurements and kernels for source-structure inversions in noise tomography. *Geophysical Journal International*, *196*(2), 971–985. <https://doi.org/10.1093/gji/ggt411>
- Hanasoge, S. M. (2013b). The influence of noise sources on cross-correlation amplitudes. *Geophysical Journal International*, *192*(1), 295–309. <https://doi.org/10.1093/gji/ggs015>
- Harmon, N., Rychert, C., & Gerstoft, P. (2010). Distribution of noise sources for seismic interferometry. *Geophysical Journal International*, *183*(3), 1470–1484. <https://doi.org/10.1111/j.1365-246X.2010.04802.x>
- Hasselmann, K. (1963). A statistical analysis of the generation of microseisms. *Reviews of Geophysics*, *1*(2), 177–210. <https://doi.org/10.1029/RG001i002p00177>
- Haubrich, R. A., & McCamy, K. (1969). Microseisms: Coastal and pelagic sources. *Reviews of Geophysics*, *7*(3), 539–571. <https://doi.org/10.1029/RG007i003p00539>
- Hejrani, B., Tkalčić, H., & Fichtner, A. (2017). Centroid moment tensor catalogue using a 3-D continental scale Earth model: Application to earthquakes in Papua New Guinea and the Solomon Islands. *Journal of Geophysical Research: Solid Earth*, *122*, 5517–5543. <https://doi.org/10.1002/2017JB014230>
- Hillers, G., Graham, N., Campillo, M., Kedar, S., Landès, M., & Shapiro, N. (2012). Global oceanic microseism sources as seen by seismic arrays and predicted by wave action models. *Geochemistry, Geophysics, Geosystems*, *13*, Q01021. <https://doi.org/10.1029/2011GC003875>
- Hinze, M., Pinnau, R., Ulbrich, M., & Ulbrich, S. (2008). *Optimization with PDE constraints*. Berlin: Springer.
- Juretzek, C., & Hadziioannou, C. (2016). Where do ocean microseisms come from? A study of Love-to-Rayleigh wave ratios. *Journal of Geophysical Research: Solid Earth*, *121*, 6741–6756. <https://doi.org/10.1002/2016JB013017>
- Kobayashi, N., & Nishida, K. (1998). Continuous excitation of planetary free oscillations by atmospheric disturbances. *Nature*, *395*(6700), 357–360.
- Komatitsch, D., & Tromp, J. (2002a). Spectral-element simulations of global seismic wave propagation, part II: 3-D models, oceans, rotation, and gravity. *Geophysical Journal International*, *150*, 303–318.
- Komatitsch, D., & Tromp, J. (2002b). Spectral-element simulations of global seismic wave propagation, part I: Validation. *Geophysical Journal International*, *149*, 390–412.
- Kurrie, D., & Widmer-Schmidrig, R. (2006). Spatiotemporal features of the Earth's background oscillations observed in central Europe. *Geophysical Research Letters*, *33*, L24304. <https://doi.org/10.1029/2006GL028429>
- Kurrie, D., & Widmer-Schmidrig, R. (2008). The horizontal hum of the Earth: A global background of spheroidal and toroidal modes. *Geophysical Research Letters*, *35*, L06304. <https://doi.org/10.1029/2007GL033125>
- Landès, M., Hubans, F., Shapiro, N. M., Paul, A., & Campillo, M. (2010). Origin of deep ocean microseisms by using teleseismic body waves. *Journal of Geophysical Research*, *115*, B05302. <https://doi.org/10.1029/2009JB006918>
- Lee, E.-J., Chen, P., Jordan, T. H., & Wang, L. (2011). Rapid full-wave centroid moment tensor (CMT) inversion in a three-dimensional Earth structure model for earthquakes in Southern California. *Geophysical Journal International*, *186*(1), 311–330. <https://doi.org/10.1111/j.1365-246X.2011.05031.x>
- Lehuteur, M., Vergne, J., Maggi, A., & Schmittbuhl, J. (2017). Ambient noise tomography with non-uniform noise sources and low aperture networks: Case study of deep geothermal reservoirs in northern Alsace, France. *Geophysical Journal International*, *208*(1), 193–210. <https://doi.org/10.1093/gji/ggw373>
- Lin, F.-C., Moschetti, M. P., & Ritzwoller, M. H. (2008). Surface wave tomography of the western United States from ambient seismic noise: Rayleigh and Love wave phase velocity maps. *Geophysical Journal International*, *173*(1), 281–298. <https://doi.org/10.1111/j.1365-246X.2008.03720.x>
- Longuet-Higgins, M. S. (1950). A theory of the origin of microseisms. *Proceedings of the Royal Society of London. Series A: Mathematical*, *243*(857), 1–35.
- Mordret, A., Landès, M., Shapiro, N. M., Singh, S. C., Roux, P., & Barkved, O. I. (2013). Near-surface study at the Valhall oil field from ambient noise surface wave tomography. *Geophysical Journal International*, *193*(3), 1627–1643. <https://doi.org/10.1093/gji/ggt061>
- Nakata, N., Chang, J. P., Lawrence, J. F., & Boué, P. (2015). Body wave extraction and tomography at Long Beach, California, with ambient-noise interferometry. *Journal of Geophysical Research: Solid Earth*, *120*, 1159–1173. <https://doi.org/10.1002/2015JB011870>
- Nawa, K., Suda, N., Fukao, Y., Sato, T., Aoyama, Y., & Shibuya, K. (1998). Incessant excitation of the Earth's free oscillations. *Earth Planets and Space*, *50*(1), 3–8. <https://doi.org/10.1186/BF03352080>
- Nishida, K. (2013). Global propagation of body waves revealed by cross-correlation analysis of seismic hum. *Geophysical Research Letters*, *40*, 1691–1696. <https://doi.org/10.1002/grl.50269>
- Nishida, K. (2014). Source spectra of seismic hum. *Geophysical Journal International*, *199*(1), 416–429. <https://doi.org/10.1093/gji/ggu272>
- Nishida, K., & Fukao, Y. (2007). Source distribution of Earth's background free oscillations. *Journal of Geophysical Research*, *112*, B06306. <https://doi.org/10.1029/2006JB004720>
- Nishida, K., & Kobayashi, N. (1999). Statistical features of Earth's continuous free oscillations. *Journal of Geophysical Research*, *104*(B12), 28,741–28,750.
- Nishida, K., Kawakatsu, H., Fukao, Y., & Obara, K. (2008). Background Love and Rayleigh waves simultaneously generated at the Pacific Ocean floors. *Geophysical Research Letters*, *35*, L16307. <https://doi.org/10.1029/2008GL034753>
- Nishida, K., Kawakatsu, H., & Obara, K. (2008). Three-dimensional crustal S wave velocity structure in Japan using microseismic data recorded by Hi-net tiltmeters. *Journal of Geophysical Research*, *113*, B10302. <https://doi.org/10.1029/2007JB005395>
- Nishida, K., Kobayashi, N., & Fukao, Y. (2000). Resonant oscillations between the solid earth and the atmosphere. *Science*, *287*(5461), 2244–2246. <https://doi.org/10.1126/science.287.5461.2244>
- Nissen-Meyer, T., Dahlen, F. A., & Fournier, A. (2007). Spherical Earth Fréchet sensitivity kernels. *Geophysical Journal International*, *168*, 1051–1066.

- Pedersen, H. A., Krueger, F., & SVEKALAPKO Array working group (2007). Influence of the seismic noise characteristics on noise correlations in the Baltic shield. *Geophysical Journal International*, 168(1), 197–210. <https://doi.org/10.1111/j.1365-246X.2006.03177.x>
- Peterson, J. (1993). *Observations and modeling of seismic background noise, U.S. Geological Survey open-file report* (Vol. 93–322, p. 94). Albuquerque: U.S. Geological Survey.
- Prieto, G. A., & Beroza, G. C. (2008). Earthquake ground motion prediction using the ambient seismic field. *Geophysical Research Letters*, 35, L14304. <https://doi.org/10.1029/2008GL034428>
- Prieto, G. A., Lawrence, J. F., & Beroza, G. C. (2009). Anelastic Earth structure from the coherency of the ambient seismic field. *Journal of Geophysical Research*, 114, B07303. <https://doi.org/10.1029/2008JB006067>
- Reading, A. M., Koper, K. D., Gal, M., Graham, L. S., Tkalčić, H., & Hemer, M. A. (2014). Dominant seismic noise sources in the Southern Ocean and West Pacific, 2000–2012, recorded at the Warramunga Seismic Array, Australia. *Geophysical Research Letters*, 41, 3455–3463. <https://doi.org/10.1002/2014GL060073>
- Retailleau, L., Boué, P., Stehly, L., & Campillo, M. (2017). Locating microseism sources using spurious arrivals in intercontinental noise correlations. *Journal of Geophysical Research: Solid Earth*, 122. <https://doi.org/10.1002/2017JB014593>
- Rhie, J., & Romanowicz, B. (2004). Excitation of Earth's continuous free oscillations by atmosphere-ocean-seafloor coupling. *Nature*, 431(7008), 552–556. <https://doi.org/10.1038/nature02942>
- Rhie, J., & Romanowicz, B. (2006). A study of the relation between ocean storms and the Earth's hum. *Geochemistry, Geophysics, Geosystems*, 7, Q10004. <https://doi.org/10.1029/2006GC001274>
- Ritsema, J., Deuss, A., van Heijst, H. J., & Woodhouse, J. H. (2011). S40RTS: A degree-40 shear-velocity model for the mantle from new Rayleigh wave dispersion, teleseismic traveltime and normal-mode splitting function measurements. *Geophysical Journal International*, 184, 1223–1236.
- Roux, P., Sabra, K. G., Kuperman, W. A., & Roux, A. (2005). Ambient noise cross correlation in free space: Theoretical approach. *The Journal of the Acoustical Society of America*, 117(1), 79–84. <https://doi.org/10.1121/1.1830673>
- Sadeghisorkhani, H., Gudmundsson, O., Roberts, R., & Tryggvason, A. (2016). Mapping the source distribution of microseisms using noise covariogram envelopes. *Geophysical Journal International*, 205(3), 1473–1491. <https://doi.org/10.1093/gji/ggw092>
- Sager, K., Ermert, L., Böhm, C., & Fichtner, A. (2017). Towards full waveform ambient noise inversion. *Geophysical Journal International*, 566–590. <https://doi.org/10.1093/gji/ggx429>
- Sánchez-Sesma, F. J., & Campillo, M. (2006). Retrieval of the Green's function from cross correlation: The canonical elastic problem. *Bulletin of the Seismological Society of America*, 96, 1182–1191.
- Saygin, E., & Kennett, B. L. N. (2012). Crustal structure of Australia from ambient seismic noise tomography. *Journal of Geophysical Research*, 117, B01304. <https://doi.org/10.1029/2011JB008403>
- Schimmel, M., Stutzmann, E., & Gallart, J. (2011). Using instantaneous phase coherence for signal extraction from ambient noise data at a local to a global scale. *Geophysical Journal International*, 184(1), 494–506.
- Schulte-Pelkum, V., Earle, P. S., & Vernon, F. L. (2004). Strong directivity of ocean-generated seismic noise. *Geochemistry, Geophysics, Geosystems*, 5, Q03004. <https://doi.org/10.1029/2003GC000520>
- Seats, K. J., Lawrence, J. F., & Prieto, G. A. (2012). Improved ambient noise correlation functions using Welch's method. *Geophysical Journal International*, 188(2), 513–523. <https://doi.org/10.1111/j.1365-246X.2011.05263.x>
- Sergeant, A., Stutzmann, E., Maggi, A., Schimmel, M., Arduin, F., & Obrebski, M. (2013). Frequency-dependent noise sources in the North Atlantic Ocean. *Geochemistry, Geophysics, Geosystems*, 14, 5341–5353. <https://doi.org/10.1002/2013GC004905>
- Seydoux, L., Shapiro, N. M., de Rosny, J., & Landès, M. (2016). Spatial coherence of the seismic wavefield continuously recorded by the USArray. *Geophysical Research Letters*, 43, 9644–9652. <https://doi.org/10.1002/2016GL070320>
- Shapiro, N. M., Ritzwoller, M., & Bensen, G. (2006). Source location of the 26 sec microseism from cross-correlations of ambient seismic noise. *Geophysical Research Letters*, 33, L18310. <https://doi.org/10.1029/2006GL027010>
- Simute, S., Steptoe, H., Cobden, L., Gokhberg, A., & Fichtner, A. (2016). Full-waveform inversion of the Japanese Islands region. *Journal of Geophysical Research: Solid Earth*, 121, 3722–3741. <https://doi.org/10.1002/2016JB012802>
- Snieder, R. (2004). Extracting the Green's function from the correlation of coda waves: A derivation based on stationary phase. *Physical Review E*, 69, 46610. <https://doi.org/10.1103/PhysRevE.69.046610>
- Specfem developers (2015). SPECFEM 3D Globe User Manual.
- Stehly, L., & Boué, P. (2017). On the interpretation of the amplitude decay of noise correlations computed along a line of receivers. *Geophysical Journal International*, 209(1), 358–372. <https://doi.org/10.1093/gji/ggx021>
- Stehly, L., Campillo, M., & Shapiro, N. M. (2006). A study of the seismic noise from its long-range correlation properties. *Journal of Geophysical Research*, 111, B10306. <https://doi.org/10.1029/2005JB004237>
- Stehly, L., Fry, B., Campillo, M., Shapiro, N., Guilbert, J., Boschi, L., & Giardini, D. (2009). Tomography of the Alpine region from observations of seismic ambient noise. *Geophysical Journal International*, 178(1), 338–350.
- Stutzmann, E., Arduin, F., Schimmel, M., Mangeney, A., & Patau, G. (2012). Modelling long-term seismic noise in various environments. *Geophysical Journal International*, 191(2), 707–722. <https://doi.org/10.1111/j.1365-246X.2012.05638.x>
- Stutzmann, E., Schimmel, M., Patau, G., & Maggi, A. (2009). Global climate imprint on seismic noise. *Geochemistry, Geophysics, Geosystems*, 10, Q11004. <https://doi.org/10.1029/2009GC002619>
- Suda, N., Nawa, K., & Fukao, Y. (1998). Earth's background free oscillations. *Science*, 279(5359), 2089–2091. <https://doi.org/10.1126/science.279.5359.2089>
- Tanimoto, T. (2005). The oceanic excitation hypothesis for the continuous oscillations of the Earth. *Geophysical Journal International*, 160(1), 276–588. <https://doi.org/10.1111/j.1365-246X.2004.02484.x>
- Tanimoto, T., Um, J., Nishida, K., & Kobayashi, N. (1998). Earth's continuous oscillations observed on seismically quiet days. *Geophysical Research Letters*, 25(10), 1553–1556. <https://doi.org/10.1029/98GL01223>
- Tape, C., Liu, Q., Maggi, A., & Tromp, J. (2009). Adjoint tomography of the Southern California Crust. *Science*, 325(5943), 988–992. <https://doi.org/10.1126/science.1175298>
- Tape, C., Liu, Q., Maggi, A., & Tromp, J. (2010). Seismic tomography of the southern California crust based upon spectral-element and adjoint methods. *Geophysical Journal International*, 180, 433–462.
- Tian, Y., & Ritzwoller, M. H. (2015). Directionality of ambient noise on the Juan de Fuca plate: Implications for source locations of the primary and secondary microseisms. *Geophysical Journal International*, 201(1), 429–443.
- Traer, J., & Gerstoft, P. (2014). A unified theory of microseisms and hum. *Journal of Geophysical Research: Solid Earth*, 119, 3317–3339. <https://doi.org/10.1002/2013JB010504>
- Traer, J., Gerstoft, P., Bromirski, P. D., & Shearer, P. M. (2012). Microseisms and hum from ocean surface gravity waves. *Journal of Geophysical Research*, 117, B11307. <https://doi.org/10.1029/2012JB009550>

- Tromp, J., Luo, Y., Hanasoge, S., & Peter, D. (2010). Noise cross-correlation sensitivity kernels. *Geophysical Journal International*, *183*, 791–819.
- Tsai, V. C. (2009). On establishing the accuracy of noise tomography traveltimes measurements in a realistic medium. *Geophysical Journal International*, *178*, 1555–1564.
- van Driel, M., Krischer, L., Stähler, S. C., Hosseini, K., & Nissen-Meyer, T. (2015). Instaseis: Instant global seismograms based on a broadband waveform database. *Solid Earth*, *6*(2), 701–717. <https://doi.org/10.5194/se-6-701-2015>
- Wapenaar, K., & Fokkema, J. (2006). Green's function representations for seismic interferometry. *Geophysics*, *71*, S133–S146.
- Weaver, R. L., & Lobkis, O. I. (2004). Diffuse fields in open systems and the emergence of Green's function. *The Journal of the Acoustical Society of America*, *116*, 2731–2734.
- Webb, S. C. (2007). The Earth's 'hum' is driven by ocean waves over the continental shelves. *Nature*, *445*(7129), 754–756.
- Webb, S. C. (2008). The Earth's hum: The excitation of Earth normal modes by ocean waves. *Geophysical Journal International*, *174*(2), 542–566. <https://doi.org/10.1111/j.1365-246X.2008.03801.x>
- Wielandt, E., & Streckeisen, G. (1982). The leaf-spring seismometer: Design and performance. *Bulletin of the Seismological Society of America*, *72*(6A), 2349–2367.
- Woodard, M. F. (1997). Implications of localized, acoustic absorption for heliotomographic analysis of sunspots. *The Astrophysical Journal*, *485*, 890–894.
- Yang, Y., & Ritzwoller, M. H. (2008). Characteristics of ambient seismic noise as a source for surface wave tomography. *Geochemistry, Geophysics, Geosystems*, *9*, Q02008. <https://doi.org/10.1029/2007GC001>
- Yang, Y., Ritzwoller, M. H., Levshin, A. L., & Shapiro, N. M. (2007). Ambient noise Rayleigh wave tomography across Europe. *Geophysical Journal International*, *168*(1), 259–274. <https://doi.org/10.1111/j.1365-246X.2006.03203.x>
- Yanovskaya, T., Koroleva, T., & Lyskova, E. (2016). Effect of earthquakes on ambient noise surface wave tomography in upper-mantle studies. *Geophysical Journal International*, *205*(2), 1208–1220. <https://doi.org/10.1093/gji/ggw083>
- Yao, H., & van der Hilst, R. D. (2009). Analysis of ambient noise energy distribution and phase velocity bias in ambient noise tomography, with application to SE Tibet. *Geophysical Journal International*, *179*, 1113–1132.
- Zheng, Y., Shen, W., Zhou, L., Yang, Y., Xie, Z., & Ritzwoller, M. H. (2011). Crust and uppermost mantle beneath the North China Craton, northeastern China, and the Sea of Japan from ambient noise tomography. *Journal of Geophysical Research*, *116*, B12312. <https://doi.org/10.1029/2011JB008637>